

GRAPE-SPH Chemodynamical Simulation of Elliptical Galaxies I: Evolution of Metallicity Gradients

Chiaki Kobayashi¹*

¹Max-Planck-Institute for Astrophysics, Karl-Schwarzschild-Str. 1, D-85741 Garching, Germany

Accepted 3rd Oct 2003; Received 3rd Mar 2003.

ABSTRACT

We simulate the formation and chemodynamical evolution of 124 elliptical galaxies by using a GRAPE-SPH code that includes various physical processes associated with the formation of stellar systems: radiative cooling, star formation, feedback from Type II and Ia supernovae and stellar winds, and chemical enrichment. In our CDM-based scenario, galaxies form through the successive merging of sub-galaxies with various masses. Their merging histories vary between a major merger at one extreme, and a monolithic collapse of a slow-rotating gas cloud at the other extreme. We examine the physical conditions during 151 merging events that occur in our simulation. The basic processes driving the evolution of the metallicity gradients are as follows: i) destruction by mergers to an extent dependent on the progenitor mass ratio. ii) regeneration when strong central star formation is induced at a rate dependent on the gas mass of the secondary. iii) slow evolution as star formation is induced in the outer regions through late gas accretion. We succeed in reproducing the observed variety of the radial metallicity gradients. The average metallicity gradient $\Delta \log Z / \Delta \log r \simeq -0.3$ with dispersion of ± 0.2 and no correlation between gradient and galaxy mass are consistent with observations of Mg₂ gradients. The variety of the gradients stems from the difference in the merging histories. Galaxies that form monolithically have steeper gradients, while galaxies that undergo major mergers have shallower gradients. Thus merging histories can, in principle, be inferred from the observed metallicity gradients of present-day galaxies. The observed variation in the metallicity gradients cannot be explained by either *monolithic collapse* or by *major merger* alone. Rather it requires a model in which both formation processes arise, such as the present CDM scheme.

Key words: methods: N-body simulations — galaxies: abundances — galaxies: elliptical and lenticular, cD — galaxies: evolution — galaxies: formation

1 INTRODUCTION

The internal structure of galaxies, spectrophotometric, chemical, and dynamical properties of various locations within a galaxy, is closely related the processes of galaxy formation and evolution. Stars in a galaxy are fossils; the star formation and chemical enrichment history of the galaxy are imprinted on their kinematics and chemical abundances. The SAURON project with William Herschel Telescope (Bacon et al. 2001) is providing the wide-field mapping of the kinematics and stellar population, which will certainly give stringent constraints on the galaxy formation and evolution. Multiobject and Integral Field Spectrographs are being developed also on 8-10m ground-based telescopes, which can give the time evolution of such internal structure. To derive the physical processes from such observational data,

it is necessary to construct a realistic model, i.e., a three-dimensional chemodynamical model, and to compare the theoretical predictions with such observational data.

Theoretical approaches have been performed in many ways: 1) The one-zone model (e.g., Tinsley 1980; Arimoto & Yoshii 1987; Matteucci 1996) played an important role in constructing the basic evolutionary scenarios of galaxies. In this model, the star formation history of a galaxy is constructed by carefully comparing the model predictions with the mean photometric and chemical properties of observed galaxies. However, because of the simplified assumption that all matter in a galaxy is well-mixed instantaneously, the one-zone model provides no idea of the internal structure of galaxies. 2) The semi-analytic model (e.g., Kauffmann, White & Guiderdoni 1993; Cole et al. 1994), which is based on the Press-Schechter theory, can provide the mass function of dark halos, their survival timescales, and the merging rates. By adopting empirical laws to de-

* E-mail: chiaki@MPA-Garching.MPG.DE

termine the stellar mass and the mass of heavy elements, and by introducing simple rules to determine the galaxy morphology (i.e., an elliptical galaxy forms from the major merger of spiral galaxies), the semi-analytic model could reproduce some correlations among global properties (e.g., the Tully-Fisher relation and color-magnitude relation) and some constraints on the number of galaxies (e.g., the luminosity function and number counts). However, there seems to be some difficulties to explain the number evolution of elliptical galaxies (e.g., Benson, Ellis & Menanteau 2002). The observed information on the internal structures remains untouched. 3) Numerical simulations of dissipationless systems (e.g., Toomre & Toomre 1972; White 1978) provide the interpretation of the interaction of galaxies and the internal structure of a galaxy. The gas dynamics in three dimensions was included in such numerical simulations (e.g., Hernquist & Katz 1989), and then star formation, feedback (Katz 1992), and chemical enrichment (Steinmetz & Müller 1994) were included. It is now possible to predict the spatial distributions of gas, stars, and heavy elements in a galaxy. However, the comparison with the observations has not been fully attempted yet. The reason is that it takes long time to calculate the evolution of one galaxy with enough resolution to predict such distributions. To reduce the calculation time and to improve the resolution, a variety of methods have been invented.

The Smoothed Particle Hydrodynamics method (SPH) is widely used to calculate three dimensional hydrodynamics with a Lagrangian scheme (Lucy 1977; Gingold & Monaghan 1977; Monaghan 1992 for a review), and has been applied to many astrophysical problems that have large density contrasts; formation of galaxies (Hernquist & Katz 1989; Navarro & White 1993; Steinmetz & Müller 1994) and a cloud-cloud collision (Lattanzio et al. 1985; Habe & Ohta 1992). Various codes have been developed to combine SPH with collisionless particles (i.e., dark matter and star particles; hereafter an N-body system) using different methods to calculate gravitational forces; direct summations, Particle-Particle/Particle-Mesh methods (Evrard 1988), Tree methods (Hernquist & Katz 1989; Benz et al. 1990), and the method using the special purpose computer GRAPE (Umemura et al. 1993; Steinmetz 1996). GRAPE (GRAvity PipE) is a special purpose computer for efficiently calculating gravitational force and potential (Sugimoto et al. 1990). The GRAPE-SPH enables us to simulate the formation and evolution of a galaxy with more than 10^4 particles in calculation time as short as a few days. It makes it possible to simulate many types of galaxies with different initial conditions, which is crucial to study the formation and evolution of galaxies statistically.

The aim of our study is to put constraints on the formation history of elliptical galaxies by comparing the observed internal structures of stellar population. To construct a self-consistent three-dimensional chemodynamical model, we have introduced various physical processes associated with the formation of stellar systems such as radiative cooling, star formation, feedback of Type II and Ia supernovae (SNe II and SNe Ia), and stellar winds (SWs), and chemical enrichment. The chemical enrichment of SNe Ia has been recently included in several chemodynamical models. Among two alternative scenarios of

the SN Ia progenitor (e.g., Kobayashi et al. 1998), most chemodynamical models (Raiteri, Villata & Navarro 1996; Carraro, Lia & Chiosi 1998) adopted Greggio & Renzini (1983)'s formulation based on the double-degenerate scenario. Mosconi et al. (2001) adopted single time delay for the SN Ia contribution, and the parameter corresponds to the double-degenerate scenario. The single-degenerate scenario has been introduced in Nakasato & Nomoto (2003) and Kawata & Gibson (2003). It may be useful to note that Woosley & Weaver (1995)'s iron yield is too large compared with the observed abundance ratios in the Milky Way Galaxy, and thus their iron yield should be reduced to be half. Such modification is always adopted in the one-zone models, but is never mentioned in many chemodynamical models. We have constructed a realistic model of chemical enrichment, excluding the instantaneous recycling approximation, including the mass-dependent yields of SNe II and the single-degenerate scenario of SNe Ia. We then solved the evolution of slowly-rotating systems that consist of dark matter, gas, and stars from various initial conditions to predict the spatial distribution of stellar population within a galaxy. By comparing the theoretical metallicity gradients with the observed ones, we discuss the origin of elliptical galaxies.

How elliptical galaxies form is a long-standing issue as a matter of big debate. The regularity in the light distribution and the global velocity anisotropy in elliptical galaxies were explained by the violent relaxation (Lynden-Bell 1967). Effectively dissipationless formation of an elliptical galaxy was discussed in various ways; e.g., stars have formed prior to the beginning of the collapse of the gas cloud (Gott 1973, 1975) or stars have formed slowly in disk galaxies which subsequently merge to make a spheroidal galaxy (Toomre 1977; Marchant & Shapiro 1977; Barnes 1988). The limit of completely dissipationless collapse is amenable to N-body experiments, which can form the objects that have the observed dynamical properties. However, the dissipation during the formation is indispensable to explain the photometric and chemical properties of elliptical galaxies such as the color-magnitude relation, the mass-metallicity relation, and the radial metallicity gradients.

Two competing scenarios of the formation of elliptical galaxies have so far been proposed: Elliptical galaxies should form monolithically by gravitational collapse of gas cloud with considerable energy dissipation (hereafter referred to as the monolithic collapse hypothesis; e.g., Larson 1974b; Arimoto & Yoshii 1987), or alternatively ellipticals should form via mergers of gaseous disk galaxies or of many dwarf galaxies (hereafter referred to as the merger hypothesis; e.g., Toomre 1977; Kauffmann et al. 1993; Baugh, Cole & Frenk 1996; Steinmetz & Navarro 2002). The merger hypothesis can be supported by the dynamical disturbances of observed ellipticals such as shells/ripples and multiple cores (Schweizer et al. 1990; Schweizer & Seitzer 1992; see also Bender & Surma 1992), and may easily explain the morphology-density relation of galaxies in clusters (Dressler 1980; Dressler et al. 1997). However, elliptical galaxies show apparently little evidence for on-going star formation, the bulk of their stars are old (e.g., Kodama & Arimoto 1997; Stanford, Eisenhardt & Dickinson 1998; Kodama et al. 1998; Silva & Bothun 1998). The monolithic collapse hypothesis assumes that the bulk of stars in ellipticals

form during an initial star burst at high redshift, and that the star formation is terminated by a supernovae-driven galactic wind that expels the left-over interstellar gas from galaxies. The galactic wind is supposed to play an essential role in injecting heavy elements into the hot intracluster gas (Ciotti et al. 1991), and predicts tight correlations among global properties of galaxies such as the color-magnitude relation (Bower, Lucey & Ellis 1992), the metallicity-velocity dispersion relation (Davies et al. 1987), and the fundamental plane (Djorgovski & Davis 1987; Dressler et al. 1987). (The color-magnitude relation could be reproduced also under the merger hypothesis (Kauffmann & Charlot 1998, but see Cole et al. 2000).) Recent observations of clusters at high redshifts reveal that these relationships exist even at $z \sim 1$ (Dickinson 1996; Schade, Barrientos & Lopez-Cruz 1997; Kelson et al. 1997; Stanford et al. 1998), which indicates that the bulk of stars in cluster ellipticals forms at the redshift $z_f \gtrsim 2.5 - 4$ (Kodama et al. 1998).

However, for cluster early-type galaxies, it has been argued that the “progenitor bias” is significant; the progenitors of the youngest low-redshift early-type galaxies drop out of the sample at high redshift (Kauffmann 1996; van Dokkum & Franz 1996, 2001). Thus the evolution of field early-type galaxies is now paid attention as the observational constraints. Franceschini et al. (1998) found that HDF-N early-type galaxies are relatively young with the formation epochs spanning $1 \lesssim z \lesssim 4$, but no evolution of field elliptical galaxies found at least $z \lesssim 1$ (Schade et al. 1999; Brinchmann & Ellis 2000; Im et al. 2002; see also Daddi, Cimatti & Renzini 2000). Drory et al. (2001) found mass evolution at $0.4 < z < 1.2$. At high redshift, the number of field red ellipticals is smaller than expected by the monolithic collapse hypothesis (Zepf 1997; Menanteau et al. 1999; Bargar et al. 1999), and there may be some global evolution that is consistent with the hierarchical clustering scenario (Fontana et al. 1999; Dickinson et al. 2003; but see Cimatti et al. 2002).

The radial metallicity gradient gives one of the most stringent constraints on the galaxy formation. Numerical simulations of the collapse of galaxies including star formation definitely predict strong radial gradients in chemical enrichment (e.g., Larson 1974a, 1975; Carlberg 1984), whereas the dissipationless collapse models predict no gradient in chemical enrichment (Gott 1973, 1975). During the collapse, gas is chemically enriched, flows inward, and forms new stars, which form the radial metallicity gradients. The metallicity gradients are observed as radial gradients of colors and spectral line indices (e.g., Faber 1973; Faber 1977; Davies, Sadler & Peletier 1993; Kobayashi & Arimoto 1999 for a review). A typical observed metallicity gradient of elliptical galaxies is $\Delta \log Z / \Delta \log r \simeq -0.3$, which is less steep than those predicted by numerical simulations of dissipative collapse (-0.35 in Larson 1974a; -1.0 in Larson 1975; -0.5 in Carlberg 1984). Furthermore, if elliptical galaxies form monolithically from a massive gas cloud, metallicity gradient should correlate with global properties of galaxies in the sense that more massive galaxies have steeper gradients (Carlberg 1984).

The observational feature of metallicity gradients is complicated and confusing because of a lack of suit-

able sample of uniform quality. It was shown that elliptical galaxies with larger values of the central Mg_2 ($\sim 5100\text{\AA}$) index tend to have steeper Mg_2 gradients (Gorgas, Efstathiou & Arag\'on-Salamanca 1990; Carollo, Danziger & Buson 1993; Gonzalez & Gorgas 1996). However, Davies et al. (1993) did not find any significant correlation between the Mg_2 gradient and σ_0 in the sample of 13 galaxies. Kobayashi & Arimoto (1999) re-studied line-strength gradients of 80 elliptical galaxies by using the indices of Mg_2 , Mg_b (5177\AA), Fe_1 (5270\AA), Fe_2 (5335\AA) and $H\beta$ (4861\AA), and found that the metallicity gradients do not correlate with any physical properties of galaxies, including central and mean metallicities, central velocity dispersions, absolute B-magnitudes, absolute effective radii, and dynamical masses of galaxies. Elliptical galaxies have different metallicity gradients, even if they have nearly identical properties such as masses, luminosities, and metallicities.

This discrepancy could be solved if mergers flatten the original gradient. Indeed numerical simulations showed that the gradient in a disk galaxy should be halved after three successive mergers of galaxies with similar size (White 1980). However, according to the dissipationless N-body experiment, the initial state is not fully wiped out during the violent relaxation phase, and N-body particles that were in the outer region of a progenitor galaxy are found in the similar location after merging events (van Albada 1982). From this point, it has been mentioned that metallicity gradients is not reduced by a merger (e.g., Barnes 1996). Simulations of both dissipative collapse and mergers leave room for improvements, because essential physical processes such as star formation, feedback of supernovae, and metal enrichment were not taken into account.

Here we simulate the chemodynamical evolution of elliptical galaxies based on the CDM picture. In the CDM cosmology, the amplitude of primordial fluctuation decreases with increasing wavelength, and the formation of structure is driven by the hierarchical clustering. Galaxies should form through the successive mergings of sub-galaxies with various masses. Contrary to the semi-analytic models, we exclude the assumption that elliptical galaxies form only from the major merger of disk galaxies. Instead we allow various merging histories for elliptical galaxies. In some cases, an elliptical galaxy forms by an assembly of gas rich small galaxies, which looks like a monolithic collapse. In other cases, the evolved galaxies with little gas merge to form an elliptical galaxy. This scenario is the midway of monolithic collapse and major merger of disk galaxies.

In this paper, we first describe the GRAPE-SPH code and the modeling of physical processes (§2). We classify simulated galaxies according to their merging histories (§3.1) and derive the present metallicity gradients (§3.2). In §3.3, we show that the scatter of the metallicity gradients comes from the difference in merging histories, and discuss the origin of elliptical galaxies by comparing with the observation. In §3.4, we examine the evolution of metallicity gradients via merging events that occur in our simulation, and manifest the dependences on mass ratios of merging galaxies, gas fractions, and induced star formation. In §4, we mention some future works and possible problems. Our conclusions are given in §5.

2 CHEMODYNAMICAL MODEL

2.1 Hydrodynamics

Here we describe the GRAPE-SPH code, which is originally written by N. Nakasato (2000), and is highly adaptive in space and time by means of individual smoothing lengths and individual timesteps. The SPH formulation used in the code is almost the same as Navarro & White (1993).

Instead of the continuity equation, the density ρ of each particle is determined from

$$\langle \rho(\mathbf{r}_i) \rangle \equiv \rho_i = \sum m_j W(r, h), \quad (1)$$

where r is defined as $r \equiv |\mathbf{r}_i - \mathbf{r}_j|$, and h denotes the symmetrized smoothing length defined as $h \equiv h_{ij} = \frac{1}{2}(h_i + h_j)$. The momentum equation is represented as

$$\frac{D\mathbf{v}_i}{Dt} = - \sum m_j \left(\frac{P_i}{\rho_i^2} + \frac{P_j}{\rho_j^2} + \Pi_{ij} \right) \nabla_i W(r, h) - (\nabla \Phi)_i. \quad (2)$$

The energy equation is represented as

$$\frac{Du_i}{Dt} = - \sum m_j \left(\frac{P_i}{\rho_i^2} + \frac{1}{2} \Pi_{ij} \right) (\mathbf{v}_i - \mathbf{v}_j) \cdot \nabla_i W(r, h) + \frac{\mathcal{H}_i - \Lambda_i}{\rho_i}, \quad (3)$$

where thermal conduction is neglected. We also use the equation of state for an ideal gas with $\gamma = 5/3$;

$$P_i = (\gamma - 1) \rho_i u_i. \quad (4)$$

The smoothing length h varies spatially, evolves with time, and is computed for each particle in every timestep. For the kernel W , a spherically symmetric spline (Monaghan & Lattanzio 1985; Monaghan 1992) is adopted. For the derivative of the kernel ∇W , the revised form by Thomas & Couchman (1992) is adopted. For the artificial viscous term Π_{ij} , we use the modified Monaghan & Gingold (1983) tensor and the shear free viscosity formulation with $\alpha = 1.0$ and $\beta = 2.0$ (Balsara 1995; Navarro & Steinmetz 1997). The heating \mathcal{H} and cooling Λ rates are described in the next session.

In the SPH code, a gas particle interacts with dark matter and star particles only by gravity. The gravitational potential Φ is given as

$$\Phi(\mathbf{r}_i) = -G \sum \frac{m_j}{\sqrt{|\mathbf{r}_i - \mathbf{r}_j|^2 + \epsilon^2}}, \quad (5)$$

where G is the gravitational constant. ϵ is the gravitational softening length, which we set $\epsilon = 0.5$ and 1.0 kpc for the high- and low- resolution, respectively. The gravity between these particles is calculated in direct summation using the GRAPE5 MUV (Mitaka Underground Vineyard) system in the National Astronomical Observatory of Japan and GRAPE6 of the University of Tokyo.

We use an individual timestep scheme with the following two steps. First, we compute the timestep of each particle Δt_e from the dynamical criteria using the velocity v and the acceleration a (Katz, Weinberg & Hernquist 1996); Δt_e is the minimum of $\frac{\eta^2 \epsilon}{|v|}$ and $\eta \sqrt{\frac{\epsilon}{|a|}}$, where η is a numerical parameter, and is set to be $\eta = 0.5$. Then, we derive the actual timestep Δt_a from the greatest power of 2 subdivision of the system timestep Δt_{sys} , which is smaller than Δt_e ; $\Delta t_a = \Delta t_{\text{sys}}/2^n \leq \Delta t_e$ (Navarro & White 1993). The system timestep is a fundamental timestep used to synchronize

all particles, and is set to be $\Delta t_{\text{sys}} = 2$ Myr. The time integration of the equation of motion is done using a leap-frog method modified for the individual timestep scheme.

2.2 Physical Processes

To simulate the formation and evolution of stellar systems from gas, we introduce various physical processes into the GRAPE-SPH code; radiative cooling, star formation, feedback of SNe II, SNe Ia, and SWs, and chemical enrichment including the mass dependence of SNe II. Here we describe the formulation and the assumptions of each physical processes.

2.2.1 Radiative Cooling

Radiative cooling is modeled using an equilibrium cooling function. If gas is primordial with no heavy elements ($[\text{Fe}/\text{H}] < -5$), we compute the cooling rates using two-body processes of H and He, and free-free emission (Katz et al. 1996). These processes are collisional excitation of neutral hydrogen (H^0) and singly ionized helium (He^+), collisional ionization of H^0 , He^0 , and He^+ , standard recombination of H^+ , He^+ , and He^{++} , dielectric recombination of He^+ , and free-free emission. We compute a lookup table, which lists $(\mathcal{H} - \Lambda)/n_{\text{H}}^2$ as a function of temperature and density. We then evaluate net cooling rates at intermediate values with cubic spline interpolation.

For metal-enriched gas ($[\text{Fe}/\text{H}] \geq -5$), we use a metallicity-dependent cooling function computed with the MAPPINGS III software by R.S. Sutherland (MAPPINGS III is the updates of MAPPINGS II that is described in Sutherland & Dopita 1993). The included processes are collisional line radiation, free-free and two-photon continuum, recombination, photoionization heating, collisional ionization, and Compton heating. Heavy elements can significantly enhance the cooling rate. At $T > 10^7$ K, Fe group line emission processes largely determine the cooling function, whereas at lower temperatures the lighter atoms such as C, O, and Ne dominate. Although the metallicity effect is small at $T \sim 10^4$ K, the cooling rate with $[\text{Fe}/\text{H}] = 0$ is ~ 100 times larger than that for the primordial gas around $T \sim 10^5$ K. The radiative cooling, and hence the star formation rate, strongly depends on the metallicity. In the table of cooling function that we use, cooling rates are given as functions of $[\text{Fe}/\text{H}]$, and the elemental abundance ratios are set to be constant for given $[\text{Fe}/\text{H}]$ according to the relations in the solar neighborhood; Galactic halo stars (i.e., $[\text{O}/\text{Fe}] = 0.5$) for $[\text{Fe}/\text{H}] \leq -1$, and the solar values for $[\text{Fe}/\text{H}] \geq 0$, and interpolated the halo and solar values for $-1 < [\text{Fe}/\text{H}] < 0$. Since the elemental abundance ratios depend on the star formation history and the inhomogeneous mixing of SNe II and Ia, the cooling tables depending on $[\text{O}/\text{Fe}]$ are required to increase the accuracy.

2.2.2 Star Formation

The treatment of star formation is similar to that in Katz (1992), which is widely used in GRAPE-SPH simulations. If a gas particle satisfies the following star formation criteria, a fractional part of the mass of the gas particle turns

to a star particle. Since an individual star particle has the mass of $10^{5-7} M_{\odot}$, it does not represent a single star, but an association of many stars.

Our star formation criteria are (1) converging flow, (2) rapid cooling, and (3) Jeans unstable on a particle scale;

$$(1) \quad (\nabla \cdot \mathbf{v})_i < 0, \quad (6)$$

$$(2) \quad t_{\text{cool}} < t_{\text{dyn}}, \quad (7)$$

$$(3) \quad t_{\text{dyn}} < t_{\text{sound}}. \quad (8)$$

Here t_{cool} , t_{dyn} , and t_{sound} are the cooling time, the dynamical time of a particle, and the sound crossing time, respectively, and are expressed as

$$t_{\text{cool}} = \frac{\rho u}{\Lambda}, \quad (9)$$

$$t_{\text{dyn}} = \frac{1}{\sqrt{4\pi G\rho}}, \quad (10)$$

$$t_{\text{sound}} = \frac{h_i}{c_s}, \quad (11)$$

where μ is the mean molecular weight, u is the specific thermal energy, and c_s is the local sound speed.

We assume that the star formation timescale is proportional to the dynamical timescale;

$$t_{\text{sf}} = \frac{1}{c} t_{\text{dyn}}, \quad (12)$$

where the star formation parameter c is set to be 1.0. With $c = 0.1$, star formation takes place slowly, which results in too blue colors compared with the observation (see §4 for more discussion). The star formation rate (SFR) is defined as

$$\frac{D\rho_*}{Dt} = -\frac{1}{t_{\text{sf}}}\rho = -\frac{c}{t_{\text{dyn}}}\rho = -c\sqrt{4\pi G}\rho^{\frac{3}{2}}, \quad (13)$$

where ρ_* is the stellar density. In other words, we adopt the Schmidt (1959) law, where the SFR is the power of the gas fraction, and the power index is $n_s = 1.5$. This is consistent with the H α observation of disk galaxies that implies $n_s = 1.3 \pm 0.3$ (Kennicutt 1989).

The star formation criteria are estimated with the time interval of Δt_{sf} , which is set to be 2 Myr. The star formation probability P for a gas particle forming stars during Δt is given by Katz (1992) as

$$P = 1 - \exp \left[-\frac{c}{t_{\text{dyn}}} \Delta t_{\text{sf}} \right] = 1 - \exp \left[-c\sqrt{4\pi G}\Delta t_{\text{sf}} \right]. \quad (14)$$

A random number between 0 and 1 is drawn to determine whether the gas particle forms stars during Δt_{sf} . If P is larger than the random number, star formation occurs. P is larger for higher density, and the typical density to form stars is higher with smaller c . For $c = 1.0$ and $c = 0.1$, most stars form in the region with $\rho \gtrsim 10^{-24}$ and 10^{-22} [g cm $^{-3}$], respectively. Practically, the lower limit of the gas density is given by c .

When the above criteria (Eq.[6-7] and Eq.[14]) are satisfied, a part of material of the gas particle turns to a star particle, which newly forms near the gas particle. We follow the scheme in Nakasato & Nomoto (2003), where the initial mass of the star particle, m_*^0 , is derived from the integration of the SFR over the time interval Δt_{sf} ;

$$m_*^0 = \rho \pi h_i^3 \left(1 - \exp \left[-\frac{c}{t_{\text{dyn}}} \Delta t_{\text{sf}} \right] \right). \quad (15)$$

2.2.3 Feedback

The evolved stars eject surrounding materials and heavy elements via stellar winds and supernova explosions. Those heat up, accelerate, and enrich the circumstellar and interstellar medium. High energy explosions like supernovae produce high temperature and low density regions in the interstellar medium. In SPH methods, the numerical accuracy for high density regions is much better than in mesh based methods, but the accuracy for low density regions is poorer. In an SPH simulation such as those of Navarro & White (1993), the numerical resolution (100-1000 pc) is larger than the typical size of supernova remnants (several tens of pc). Thus, because of the nature of the SPH method and the lack of resolution in current computing resources, it is necessary to simplify the release of the energy, momentum, and mass from stars. We therefore assume that energy and heavy elements that are ejected from a star particle are equally distributed to the surrounding gas particles within a sphere of feedback radius r_f , which is a parameter that controls the mixing of heavy elements. We set $r_f = 1$ kpc, which gives a good fit to the chemical evolution in the Milky Way Galaxy (Kobayashi 2002).

In this paper, we distribute the feedback energy in purely thermal form. Navarro & White (1993) proposed that the energy produced by a supernova explosion is distributed to neighbor gas particles of the star particle mostly as a thermal energy and the rest is distributed as a velocity perturbation to the gas particles; the fraction of energy in kinetic form is given by a free parameter f_{kin} . With $f_{\text{kin}} > 0$, star formation efficiency is smaller, surface brightness decreases at the center, and metal-rich gas blow out. If we adopt $f_{\text{kin}} = 0.1$, the effective radius is too large and the metallicity gradient is too shallow (see Fig.14 in §4).

The energy ejection rate E_e from a star particle as a function of age t is

$$E_e(t) = m_*^0 (e_{e,\text{SW}} \mathcal{R}_{\text{SW}}(t) + e_{e,\text{II}} \mathcal{R}_{\text{II}}(t) + e_{e,\text{Ia}} \mathcal{R}_{\text{Ia}}(t)). \quad (16)$$

\mathcal{R}_{SW} , \mathcal{R}_{II} , and \mathcal{R}_{Ia} are the rates of SWs, SNe II, and SNe Ia, respectively, of which formulations are described in §2.2.4.

The energy of SWs from solar metallicity stars is estimated to be typically 0.2×10^{51} erg from the observation of OB associations (Abbott 1982). Although there should be a mass dependence where massive stars eject larger energies, we adopted the typical value because of lack of observation. The chemical abundance of the star significantly affects SWs as $\dot{M} \propto Z^{0.8}$ (Leitherer, Robert & Drissen 1992), thus we include the metallicity effect for very massive stars;

$$e_{e,\text{SW}} = \begin{cases} 0.2 \times 10^{51} \left(\frac{Z}{Z_{\odot}} \right)^{0.8} & (m_{2,u} < m \leq m_u) \text{ [erg]}, \\ 0.2 \times 10^{51} & (m_{2,\ell} < m \leq m_{2,u}) \end{cases} \quad (17)$$

where Z is the metallicity of the star particle (see §2.2.4 for the upper and lower mass limits).

Since there are supernovae with 10 times larger energy than typical supernovae, hypernovae, the energy of all supernovae should not be the same. However, since the energy distribution function of supernovae has not been established, we adopt typical values of

$$e_{e,\text{II}} = 1.4 \times 10^{51} \quad (m_{2,\ell} < m \leq m_{2,u}) \text{ [erg]} \quad (18)$$

and

$$e_{e,\text{Ia}} = 1.3 \times 10^{51} \quad (m_{1d,\ell} < m \leq m_{1d,u}) \quad [\text{erg}] \quad (19)$$

for SNe II (Blinnikov et al. 2000) and SNe Ia (Nomoto et al. 1984), respectively (see §2.2.4 for the upper and lower mass limits).

2.2.4 Chemical Enrichment

A star particle is not a single star but an association of many stars. We assume that a star particle is in fact a simple stellar population, which is defined as a single generation of coeval and chemically homogeneous stars of various masses, i.e., it consists of a number of stars with various masses but the same age and metallicity. The mass, mass of heavy elements, and the spectral energy distribution of the star particle evolve as massive stars die. From dying stars, gas is ejected into interstellar medium by SWs, SNe II, and SNe Ia.

The mass of the stars associated with each star particle is distributed according to an initial mass function (IMF). The IMF is assumed to be invariant to time and metallicity as

$$\phi(m) \propto m^{-x}, \quad (20)$$

which is normalized to unity at $m_\ell \leq m \leq m_u$. Theoretical arguments indicate that the IMF originates from fragmentation of a gas cloud almost independently of local physics in the gas (Low & Lynden-Bell 1976; Silk 1977). In the solar neighborhood, the Salpeter IMF with $x = 1.35$ (Salpeter 1955) is a good approximation to the star counts, and gives a good fit to many properties of disk galaxies (Kennicutt 1983). For ellipticals, the flatter IMF is favored to explain the red colors of giant ellipticals (Kodama 1997). We then adopt $x = 1.10$ with the upper and lower masses of $m_\ell = 0.05M_\odot$ and $m_u = 120M_\odot$.

The ejection rates of the mass and heavy element i (E_m and E_{z_i}) from the star particle are expressed as

$$E_m(t) = m_*^0 (e_{m,\text{SW}}(t) + e_{m,\text{II}}(t) + e_{m,\text{Ia}}(t)), \quad (21)$$

and

$$E_{z_i}(t) = m_*^0 (e_{z_i,\text{SW}}(t) + e_{z_i,\text{II}}(t) + e_{z_i,\text{Ia}}(t)). \quad (22)$$

The ejection rates per mass are given by the following equations;

$$e_{m,\text{SW}} = \left(\frac{Z}{Z_\odot} \right)^{0.8} \int_{\max[m_{2,u}, m_t]}^{m_u} (1 - w_m) \phi(m) dm, \quad (23)$$

$$e_{m,\text{II}} = \int_{m_t}^{m_{2,u}} (1 - w_m) \phi(m) dm, \quad (24)$$

and

$$e_{m,\text{Ia}} = m_{\text{CO}} \mathcal{R}_{\text{Ia}}(t). \quad (25)$$

Time dependence is in the lower mass limit for integrals, the turn-off mass m_t , which is the mass of the star with the main-sequence lifetime $\tau_m = t$. For simplicity, the lifetime is determined as (David, Forman & Jones 1990)

$$\log \tau_m = 10.0 + (-3.42 + 0.88 \log m) \log m, \quad (26)$$

which gives a little (1.5 times) longer lifetime for $m \gtrsim 20M_\odot$ compared with the metallicity-dependent lifetime of Kodama & Arimoto (1997). In SWs and SNe II, stars eject the

envelope materials outside the remnants. w_m is the remnant mass fraction, which is the mass fraction of a black hole, a neutron star, or a white dwarf, depending on the initial mass m . For SNe Ia, all of the evolved He core (i.e., C+O white dwarfs) is ejected, and the mass of the white dwarf at the SN Ia explosion is $m_{\text{CO}} = 1.38M_\odot$.

Heavy elements are also ejected at the following rates;

$$e_{z_i,\text{SW}} = \left(\frac{Z}{Z_\odot} \right)^{0.8} \int_{\max[m_{2,u}, m_t]}^{m_u} (1 - w_m - p_{z_i m, \text{II}}) Z_i \phi(m) dm, \quad (27)$$

$$e_{z_i,\text{II}} = \int_{\max[m_{2,\ell}, m_t]}^{m_{2,u}} p_{z_i m, \text{II}} \phi(m) dm \quad (28)$$

$$+ \int_{\max[m_{2,\ell}, m_t]}^{m_{2,u}} (1 - w_m - p_{z_i m, \text{II}}) Z_i \phi(m) dm, \quad (29)$$

and

$$e_{z_i,\text{Ia}} = m_{\text{CO}} p_{z_i m, \text{Ia}} \mathcal{R}_{\text{Ia}}(t). \quad (30)$$

In SWs and SNe II, the heavy elements in the envelope are ejected. In SNe II and SNe Ia, the explosive nucleosynthesis takes place, and heavy elements are newly produced. $p_{z_i m, \text{II}}$ and $p_{z_i m, \text{Ia}}$ are the stellar yields, which are the mass fractions of newly produced and ejected heavy elements i , and are given from the supernovae nucleosynthesis model (Nomoto et al. 1997ab) with $p_{z_i m, \text{II}} = 0$ for $m < 10M_\odot$. The upper and lower limits of SNe II are $m_{2,u} = 50M_\odot$ and $m_{2,\ell} = 8M_\odot$, respectively. For stars with $50 - 120M_\odot$, all mass of He core turns to a black hole. Although some metals such as carbon are produced in SWs, we here neglect them because their contribution is much smaller than that of supernovae. The dependence of w_m , $p_{z_i m, \text{II}}$ and $p_{z_i m, \text{Ia}}$ on the stellar metallicity has not been included.

The rates of SWs and SNe II, \mathcal{R}_{SW} and \mathcal{R}_{II} , are obtained as

$$\mathcal{R}_{\text{SW}} = \int_{\max[m_{2,u}, m_t]}^{m_u} \frac{1}{m} \phi(m) dm, \quad (31)$$

and

$$\mathcal{R}_{\text{II}} = \int_{\max[m_{2,\ell}, m_t]}^{m_{2,u}} \frac{1}{m} \phi(m) dm. \quad (32)$$

For the SN Ia rate \mathcal{R}_{Ia} , there are several alternative role debate. Here we adopt an SN Ia model based on the single degenerate scenario including metallicity effects (Kobayashi et al. 1998; Kobayashi, Tsujimoto & Nomoto 2000);

$$\mathcal{R}_{\text{Ia}} = b \int_{\max[m_{1p,\ell}, m_t]}^{m_{1p,u}} \frac{1}{m} \phi(m) dm \quad (33)$$

$$\times \int_{\max[m_{1d,\ell}, m_t]}^{m_{1d,u}} \frac{1}{m} \phi_d(m) dm. \quad (34)$$

The primary star is a C+O white dwarf (WD) formed from a stars with initial mass between $m_{1p,\ell} = 3M_\odot$ and $m_{1p,u} = 8M_\odot = m_{2,\ell}$. This SN Ia scenario has two types of secondary stars, main-sequence (MS) and red-giant (RG) stars. We calculate the SN Ia rate for each binary system (i.e., the MS+WD and the RG+WD system) with respective b , $m_{1d,\ell}$, and $m_{1d,u}$, and combine them. The mass ranges of the companion stars are given by the simulation of binary

evolution, and are $0.9 - 1.5 M_{\odot}$ for the RG+WD system and $1.8 - 2.6 M_{\odot}$ for the MS+WD system. Thus the lifetime of SNe Ia is $\sim 2 - 20$ Gyr and $0.5 - 1.5$ Gyr, respectively. b is the binary parameters, which is the fraction of white dwarfs that eventually produce SNe Ia, and we adopt the same value which are determined from the chemical evolution in the solar neighborhood; $[b_{\text{RG}}, b_{\text{MS}}] = [0.02, 0.05]$ (Kobayashi, Tsujimoto & Nomoto 2000).

The photometric evolution of a star particle is identical to the evolution of the simple stellar population, of which spectra f_{λ} are taken from Kodama & Arimoto (1997) as a function of age t and metallicity Z . The absolute magnitude is calculated by using passbands to the the photometric system, which are the same as Kodama (1997).

2.3 Initial Condition

A cosmological initial condition is generated with the following three steps. Throughout the paper, we set the cosmological parameters of $H_0 = 50 \text{ km s}^{-1} \text{ Mpc}^{-1}$, $\Omega_m = 1.0$, $\Omega_{\Lambda} = 0$, and $\sigma_8 = 1.0$. (In the following, lengths and masses are for $H_0 = 50$.) First, we generate a periodic boundary condition with the lattice size 5 Mpc having a top-hat perturbation of amplitude 1σ or 3σ in radius 1.25 Mpc by using the COSMICS package (Bertschinger 1995). This package uses the standard Zel'dovich approximation (Zel'dovich 1970; Efstathiou et al. 1985) to compute the displacements and velocities of the dark matter particles from a Gaussian random density field. The power spectrum of this density field represents the CDM spectrum for the above cosmological parameters. To generate constrained density field, a path integral method is used (Bertschinger 1987). We set the parameters in COSMICS to get the density field realization with the desired number, mass, and the starting redshift of $z \sim 25$. By changing the seed for the random number generator, we obtain a different density field. Giving the seed at random, we obtain a random sample of initial conditions.

Second, we pick up particles in a spherical region with the comoving radius of ~ 1.5 Mpc, the mass of $\sim 10^{12} M_{\odot}$ (baryon fraction of 0.1), and N_{tot} particles (the half for gas and the rest for dark matter). In this paper, we set two different resolutions; $N_{\text{tot}} \sim 10000$ and 60000 . The mass of a dark matter particle is $\sim 1.8 \times 10^8 M_{\odot}$ and $\sim 3.0 \times 10^7 M_{\odot}$, and the mass of a gas particle is $\sim 2.0 \times 10^7 M_{\odot}$ and $\sim 3.3 \times 10^6 M_{\odot}$, respectively.

Third, we give the initial angular momentum to the system in rigid rotation because the simulated field is not enough large to generate tidal torque. The typical spin parameter of a virialized halo in CDM cosmology ranges from 0.01 to 0.1 and the median is 0.05 according to the numerical simulations (e.g., Warren et al. 1992). We adopt the constant spin parameter λ as small as ~ 0.02 . With larger λ , a spiral galaxy form if the galaxy does not undergo a major merger. If a major merger occurs, an elliptical galaxy form, even if the spin parameter is initially set to be as large as $\lambda \sim 0.1$. Thus, we should note that such ellipticals are not included in our sample (see §4 for more discussion). We also add the corresponding Hubble velocity to the velocity field of the sphere since the equation of motion is integrated not in comoving units but in physical units.

This scheme is similar to that in Katz (1992), and has been used in many works (e.g., Steinmetz & Müller

Table 1. Number of simulated galaxies

	run	ellipticals	dwarfs
high resolution ($N \sim 60000$)	13	18	0
low resolution ($N \sim 10000$)	59	60	46
total	72	78	46

1994; Nakasato & Nomoto 2003; Kawata & Gibson 2003). Simulations from true CDM initial conditions excluding the artificial boundary effect were firstly carried out by Navarro & White (1994). We should keep in mind the boundary effect of our initial condition; materials in the outside of the simulated sphere is neglected, which makes the artificial cut off of the mass accretion (see §4 for more discussion).

3 RESULTS

3.1 EVOLUTION HISTORIES

We simulate the chemodynamical evolution of 72 fields with different cosmological initial conditions (see §2.3). It takes ~ 10 days to simulate one field with high-resolution (the number of particles $N \sim 60000$), and 1 day with low-resolution ($N \sim 10000$). By the present time (i.e., $t = 13.2$ Gyr, $z = 0$), in 42 cases one galaxy forms in the center of the field, in 16 cases one galaxy and several subgalaxies, and in 14 cases a few galaxies with comparable masses. We select galaxies having stellar masses in a 20 kpc sphere larger than $4.5 \times 10^7 M_{\odot}$. Although many less-massive subgalaxies form, we discard them because our resolution is not enough to study them in detail. We summarize the number of runs and the resulting galaxies in Table 1.

Figure 1 shows the V-luminosity distributions in ± 10 kpc of 124 simulated galaxies. Luminosities are projected on the X - Y plane (the rotational axis is Z), and smoothed over 0.3 kpc. The number on the top of each image is the ID number in our simulation. The galaxies with the same number are in the same simulated field. The character “H” and “L” respectively denotes the high- and low- resolution, and the following “1” and “3” respectively denotes the 1σ and 3σ over-dense regions. The 18 galaxies in the left side are obtained with high-resolution simulations, which clearly show triaxial distributions. The stellar masses span in the range $\sim 10^{8-11} M_{\odot}$, and cD galaxies are not included in our sample. Among the 124 galaxies, 78 bright galaxies are elliptical galaxies, which have de Vaucouleurs' surface brightness profiles. Since the initial angular momentum is set to be small (spin parameter $\lambda \sim 0.02$), no spirals form. The remaining 46 faint galaxies are either dwarf ellipticals or dwarf irregular galaxies, all of which have small stellar masses as $M \lesssim 10^9 M_{\odot}$. Some dwarf galaxies show bright central cores, while others are diffusely distributing stellar systems.

Different galaxies undergo different evolution histories. The difference is seeded in the initial condition. Galaxies form through the successive merging of subgalaxies with various masses, which varies between a major merger at one extreme and a monolithic collapse of slowly-rotating gas cloud at the other. We show examples of the two cases from the high-resolution simulations in Figures 2 and 3, which

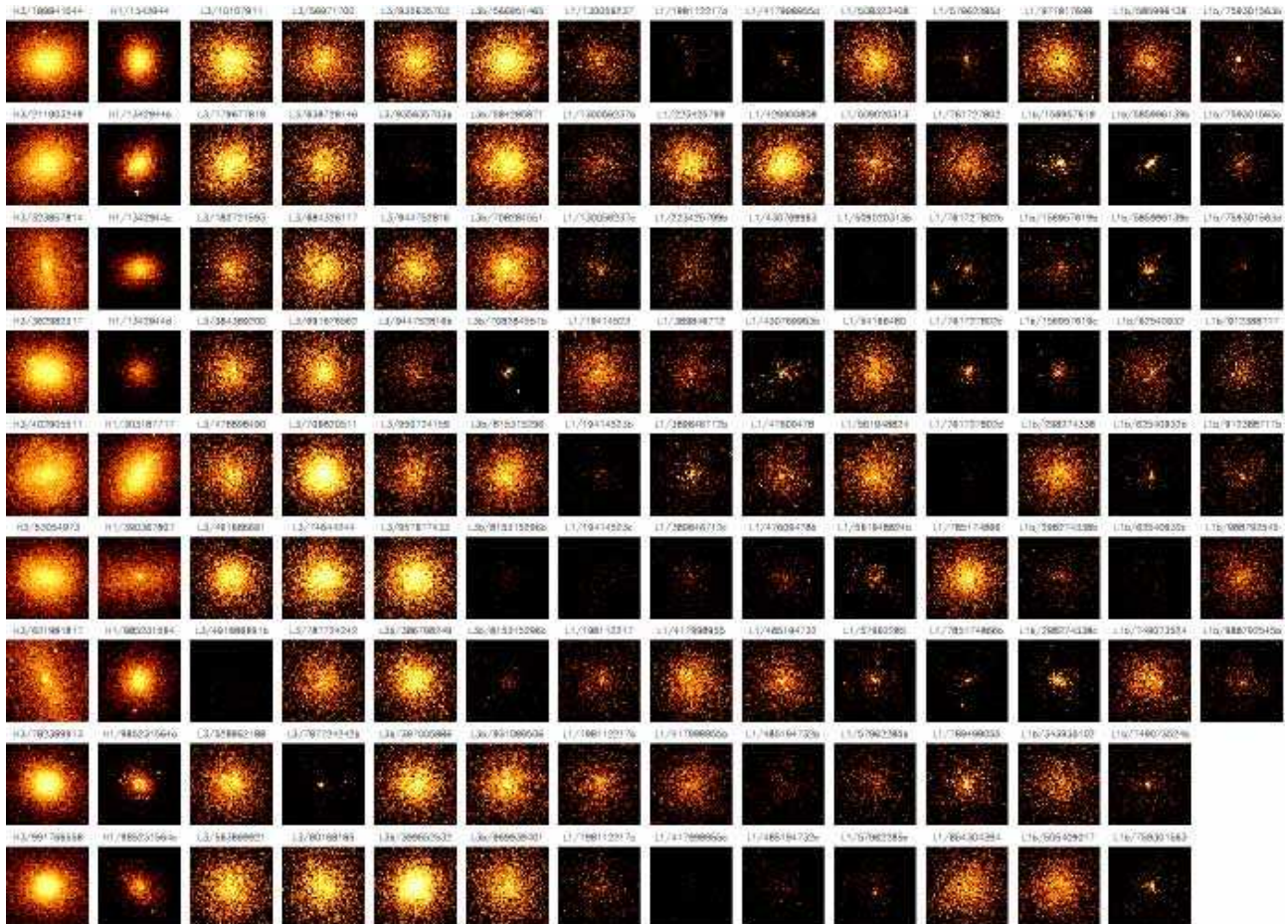


Figure 1. V-luminosity distributions in ± 10 kpc of 124 simulated galaxies with the stellar masses of $\sim 10^{8\text{--}11} M_{\odot}$. The number on the top of each image is ID number in the simulation.

show the evolution in ± 100 kpc on the X - Z plane of dark matter (first lines), gas (second lines), stars (third lines), V-luminosity (forth lines), luminosity weighted stellar metallicity (fifth lines) of galaxies that form through monolithic collapse and through major merger, respectively.

Figure 2 shows the evolution of a galaxy (ID H3/782389913) that forms monolithically. At the beginning, the system expands according to the Hubble flow. The CDM initial fluctuation produces the structures of nodes and filaments. Gas cores form in the nodes, and stars form in the gas cores. The surface brightness is as high as 14 mag arcsec $^{-2}$ in rest-frame V-band. Gas rich subgalaxies merge with one another, and the protogalaxy coalesces at $z \gtrsim 3$. The accretion of small subgalaxies continues till $z \sim 2$, and after this no significant event happens. There is only small amount of star formation at $z \lesssim 0.5$, and the luminosity of the galaxy decreases gradually toward $z = 0$.

Figure 3 shows the evolution of a galaxy (ID H3/402905511) that undergoes a major merger at $z \simeq 2.0$. The primary galaxy forms in a large gas core at $z \gtrsim 3$. The secondary galaxy forms at the same time about 200 kpc away, which comes to the center because of gravity, and merges with the primary galaxy. The secondary initially passes through the primary ($z = 1.9$), and then oscillates decreasing in mass until the system is relaxed at $z = 0.9$. We should note that the edge of the dark matter distribution

can be seen to fall onto the central object at $z \sim 6.8$ (Fig.2) and 5.0 (Fig.3). This means that the mass accretion after then may be underestimated.

We classify elliptical galaxies into the following 5 classes according to their merging histories.

[1] **Monolithic**— Galaxies form through the assembly of many ($\gtrsim 10$) gas-rich subgalaxies with the stellar masses of $M \sim 10^9 M_{\odot}$. Such assembly generally has finished by $z \sim 3$, at least by $z \sim 2$. The gas fractions (i.e., the mass ratio of gas to baryon $f_g \equiv M_g/(M+M_g)$) of merging galaxies are larger than 0.5. The material of subgalaxies quietly accretes on the central galaxy. It is difficult to discriminate these subgalaxies, and this assembly looks like a monolithic collapse.

[2] **Assembly**— Galaxies form through the assembly of subgalaxies with $M \sim 10^{10} M_{\odot}$. The gas fractions f_g of subgalaxies are as large as 0.4. Each subgalaxy has an evolved core, which violently merges with the others. While the subgalaxy passes through the central galaxy many times, many stars of the galaxy are stripped and some of them accrete on again.

[3] **Minor merger**— The formation of the main component of the present-day galaxy is the same as above two classes, but these galaxies undergo minor merger events at $z \lesssim 3$. We define the minor merger when the stellar mass

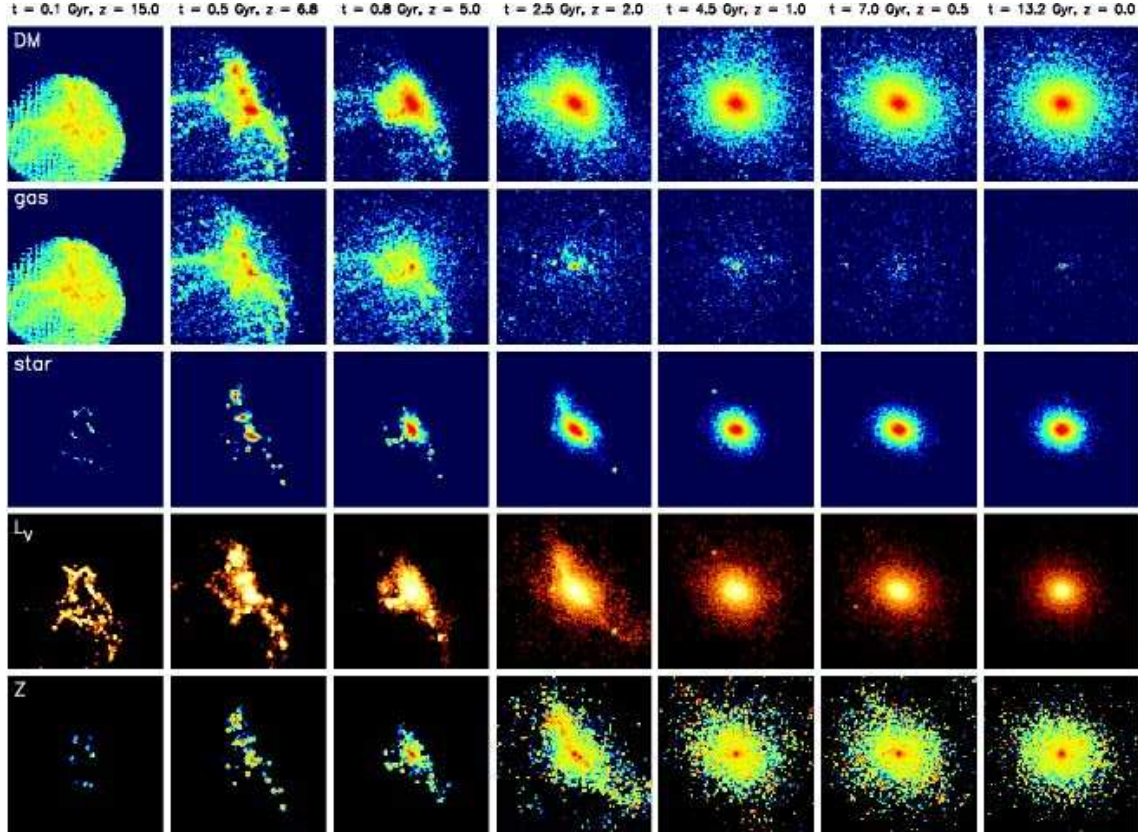


Figure 2. The evolutions in ± 100 kpc of dark matter (first lines), gas (second lines), stars (third lines), V-luminosity (forth lines), and stellar metallicity (fifth lines) of the galaxy that forms monolithically. The metallicity range is $\log Z/Z_{\odot} = -1$ to 0.4.

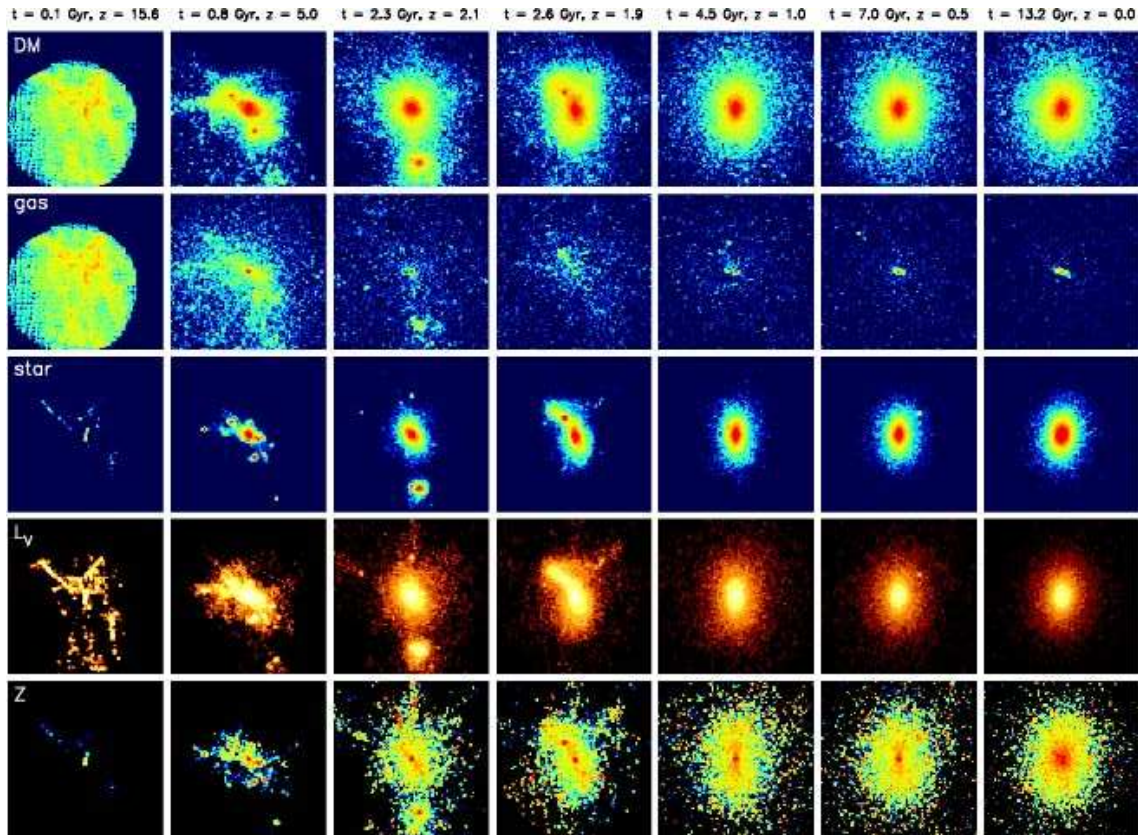


Figure 3. The same as Figure 2, but for the galaxy that undergoes a major merger at $z \approx 2.0$.

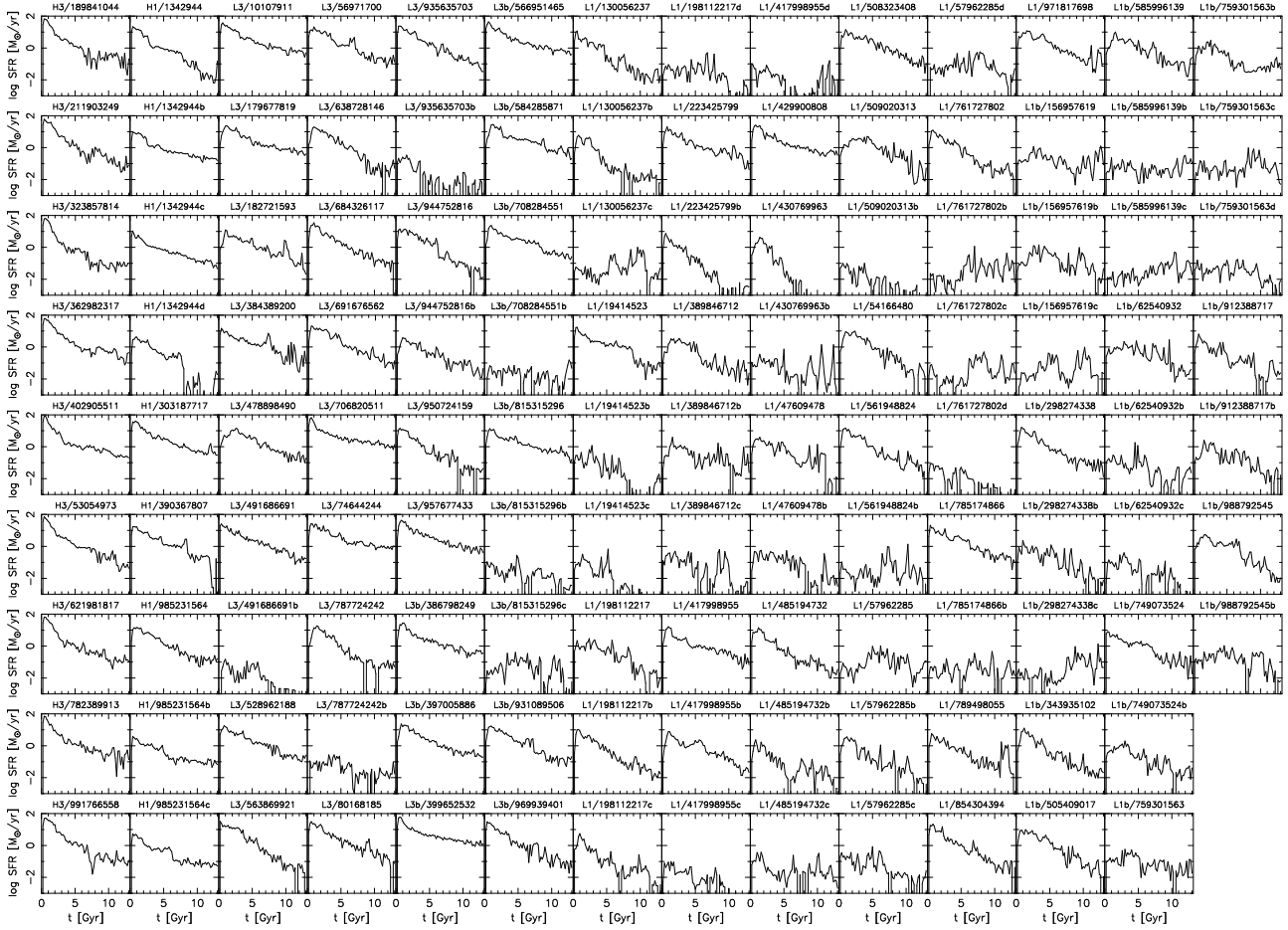


Figure 4. The star formation rates ($\log \text{SFR} [M_{\odot} \text{ yr}^{-1}]$) as functions of time t [Gyr] in a present-day galaxies ($r \leq 20$ kpc and $|Z| \leq 100$ kpc).

ratio of the merging galaxies $f \equiv M_2/M_1$ ($M_1 \geq M_2$) ranges from ~ 0.01 to ~ 0.2 . With such minor merger events, the surface brightness profile and the metallicity gradients are not affected so much.

[4] **Major merger**—Galaxies undergo the major merger with $f \gtrsim 0.2$ at $z \lesssim 3$. The mass of the primary galaxy is no more than five times larger than the mass of the secondary galaxy. The redshift $z \sim 3$ generally corresponds to the galaxy formation epoch, and the main component of the present-day galaxy forms at $z \gtrsim 3$. Thus, the major merger occurs after the most stars in the present-day galaxies formed. The merger event destroys the metallicity gradient that has existed in pre-merger galaxy in a way depending on the mass ratio f and the gas mass of the secondary galaxy (see §3.3).

[5] **Multiple major mergers**—Galaxies undergo a major merger ($f \gtrsim 0.2$) and one or two other mergers with $f \gtrsim 0.1$.

Dwarf galaxies are classified into the following 4 classes according to their star formation histories. Observationally, the first class of galaxies are dwarf ellipticals, the others are dwarf irregulars.

[D1] **Initial star burst**—Galaxies form with the initial star burst at $z \gtrsim 1$. In some galaxies, many supernova explosions occur and cause the galactic winds. In other galax-

ies, the gas is not ejected completely, but the gas density is so small that only few stars form at lower redshifts. Thus the colors are red, and these dwarfs follow the same color-magnitude relation as giant ellipticals.

[D2] **Continuous star formation**—Galaxies grow through continuous star formation. After the initial star burst, there are the accretion of gas clumps and/or the interaction with other galaxies, which make the star formation continue to lower redshifts.

[D3] **Continuous star formation with recent star burst**—The same as [D2], but a star burst occurs at the recent $2 - 3$ Gyr. Thus the galaxy colors are blue.

[D4] **Recent star burst**—Galaxies form through recent star bursts at $z \sim 0.7$. Such star bursts are induced by gas accretion and/or galaxy interactions. The colors are blue, and it is impossible to distinguish [D3] and [D4] with colors alone.

The number of galaxies in each class is [1] 5 (4.0%), [2] 18 (15%), [3] 19 (15%), [4] 25 (20%), [5] 11 (8.9%), [D1] 20 (16%), [D2] 13 (10%), [D3] 9 (7.3%), and [D4] 4 (3.2%). The percentages of non-major merger ([1]-[3]) and major merger galaxies ([4]-[5]) are 34% and 29%, respectively. We should note that the number of merger galaxies tends to be underestimated because of the boundary effect of our initial condition.

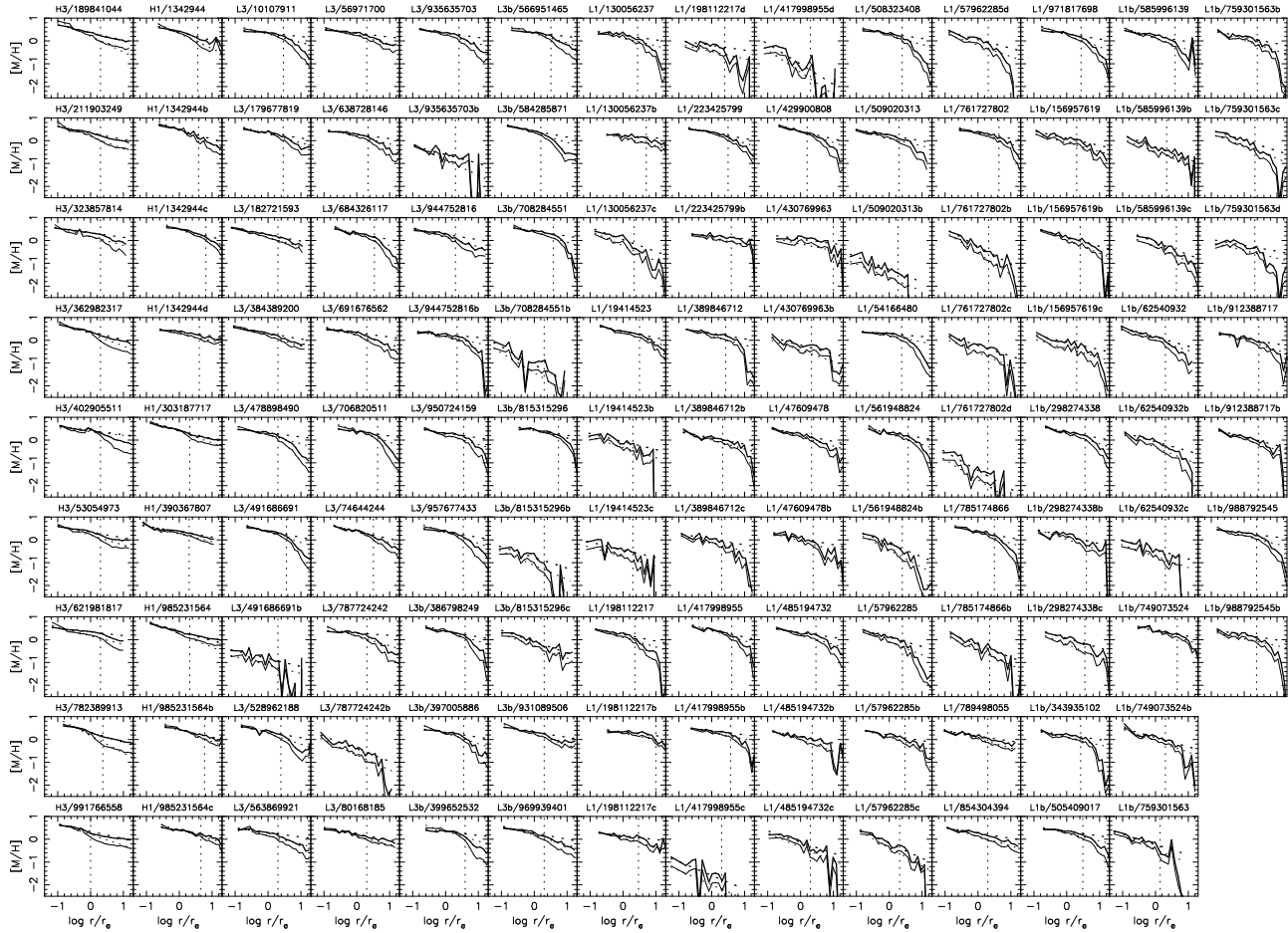


Figure 5. The metallicity gradients, where $[M/H]$ is plotted against $\log r/r_e$. The thick and thin lines show the oxygen and iron abundance gradient, respectively. The fitting lines are shown with the dotted lines. The dotted vertical lines show the maximum radii used in the fitting.

Figure 4 shows the star formation rates ($\log \text{SFR} [M_\odot \text{yr}^{-1}]$) as a function of time t [Gyr], which are derived from the ages and masses of stars that belong to the galaxy at present. Thus, these rates are not for stars formed in the region that is defined as the galaxy at each redshift, but for stars that formed anywhere and are today part of the galaxy. This definition of the SFR will be the same as in any observation that estimates the star formation history of a galaxy from its stellar populations. As clearly shown, all elliptical galaxies form with an initial star burst at $z \gtrsim 2$, whereas dwarf galaxies undergo relatively continuous star formation. The SFR decreases because the gas is exhausted in the galaxy. The secondary star burst is induced by the accretion of gas clumps and/or the merging of gas-rich galaxies. Not all merging events induce a secondary star burst; the fraction of merging events that induce such a star burst is about 10%. For all ellipticals, the initial star burst is always larger than the secondary one. The typical timescale of initial star burst is found to be 1–2 Gyr, which is much longer than the 0.1 Gyr that is commonly adopted in the one-zone model (e.g., Kodama & Arimoto 1997). Such SFR is due to the artificial cut-off of mass accretion caused by our initial condition, but is required from the observation of ellipticals as summarized in §1.

We should note that star formation has not completely

stopped at present in most elliptical galaxies. Galactic winds are hard to generate in our simulated giant ellipticals (see §4 for more discussion). At the center of the present-day galaxy, the dynamical potential is so deep that the gas density is high. In such regions, super metal-rich stars ($Z \sim 10Z_\odot$) form in the simulation. In several dwarf galaxies with $M \lesssim 10^9 M_\odot$ (e.g., ID L1/223425799b and L1/430769963), weak galactic winds can be seen even if $f_{\text{kin}} = 0$. However, enough gas is heated up and blows away gradually by the input of thermal energy of supernovae. The global gas fraction of the simulated fields spans over 50–90%, and the gas fraction in a galaxy (a sphere of $2r_e$) is 1–10% and 30–80% for giants and dwarfs, respectively. The fraction of heavy elements locked into stars in a galaxy spans 20–40% which is consistent with the observation (e.g., Renzini 2002).

3.2 METALLICITY GRADIENTS

Galaxies are observed in projection on the sky. In order to compare the simulated results with observation, foreground and background particles should be excluded properly. We define a galaxy as the projection of $|Z| \leq 100$ kpc on the X - Y plane. Below radius r means a projected radius. We then derive the effective radius r_e by fitting a de Vaucouleurs' law to the surface brightness profile. For the simulated galaxies,

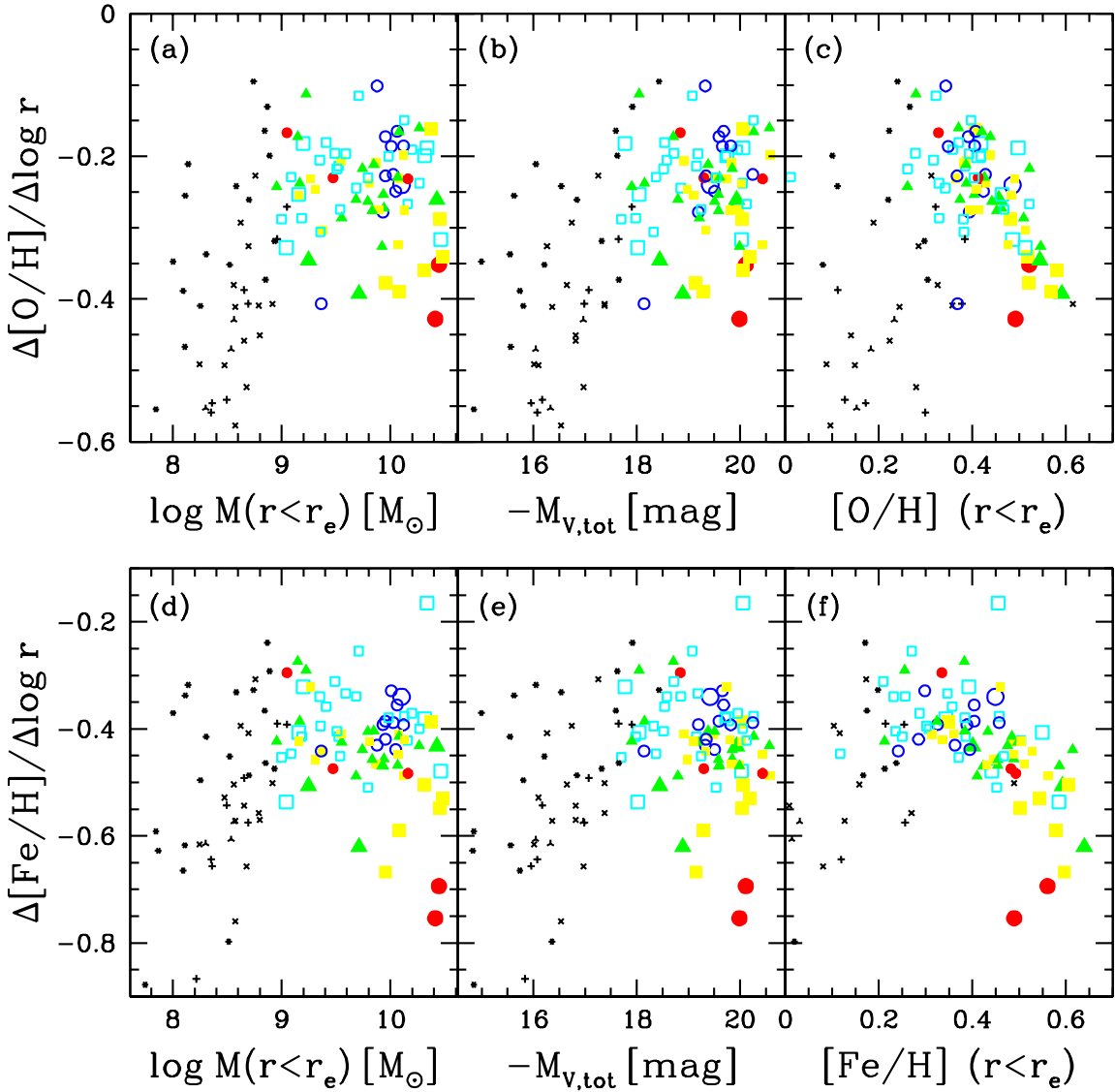


Figure 6. Metallicity gradients versus (a,d) stellar masses in r_e , (b,e) total luminosities, and (c,f) mean stellar metallicities in r_e . The upper (a-c) and lower panels (d-f) show the gradients of oxygen and iron abundances, respectively. All points are for the simulated galaxies, and the large points denote galaxies simulated with high-resolution. The shape of symbols show the merging histories for elliptical galaxies and star formation histories for dwarf galaxies; [1] monolithic (red filled circles), [2] assembly (yellow filled squares), [3] minor merger (green filled triangles), [4] major merger (cyan open squares), and [5] multiple major merger (blue open circles); [D1] initial star burst (asterisks), [D2] continuous star formation (crosses), [D3] continuous star formation with recent star burst (plus), and [D4] recent star burst (three-pointed stars).

we exclude the central region with $r = 0 - 1$ kpc and $0 - 2$ kpc when fitting simulations with high- and low- resolution, respectively, because the surface brightness is smeared out due to the softening of the gravity. In the outer region, to derive proper effective radii in the simulation, we use large enough regions such as $40 - 80$ kpc. In some case that galaxies show a local excess in the surface brightness because of the existence of the satellite subgalaxies, we only use the inner part.

Observationally, metallicity gradients are derived from the line-strength gradients, and line-strength is converted to

metallicity using an index-metallicity relation derived from spectral synthesis models (e.g., Kodama & Arimoto 1997). Thus the observed metallicity is the luminosity weighted metallicity. In the observational data, the gradients are smeared out due to poor seeing conditions at galaxy centers with $\log r/r_e \lesssim -1.5$, and in the outer regions with $\gtrsim 2r_e$ errors arising from the sky subtraction give poor fits. Kobayashi & Arimoto (1999) excluded these regions from the fitting. In the simulation, we provide the metallicity weighted by V-luminosity, because the absorption indices usually observed such as Mg₂ and Fe₁ are in the V-band.

Since we find no significant difference in the metallicity gradients at $r = 1 - 2$ kpc for the high- and low-resolutions, the innermost boundary of the fitting region is set at 1 kpc for both resolutions. This value is larger than the radius of $\log r/r_e \sim -1.5$. The outer boundary is set at $2r_e$ for most galaxies, and at 10 kpc for galaxies in the case with small r_e . The contribution of satellite galaxies is also excluded.

Figure 5 shows the metallicity gradients of 124 galaxies, where $[\text{M}/\text{H}]$ is plotted against $\log r/r_e$. The thick and thin lines show the oxygen and iron abundance gradient, respectively. The fitting lines are shown with the dotted lines. The dotted vertical lines show the maximum radii used in the fitting. As is clearly seen, the metallicity gradients are various, some are steep and others flat.

3.3 RELATION AGAINST MASS?

Figure 6 shows the V-luminosity weighted metallicity gradients versus stellar mass within r_e (a and d), total luminosities derived from the de Vaucouleurs' law (b and e), and luminosity weighted mean stellar metalicities in r_e (c and f). The upper (a-c) and lower panels (d-f) show the gradients of oxygen and iron abundances, respectively. All points are for the simulated galaxies, and the large points denote galaxies simulated with high-resolution. The symbols show the merging histories for elliptical galaxies and star formation histories for dwarf galaxies; [1] monolithic (filled circles), [2] assembly (filled squares), [3] minor merger (filled triangles), [4] major merger (open squares), and [5] multiple major merger (open circles); [D1] initial star burst (asterisks), [D2] continuous star formation (crosses), [D3] continuous star formation with recent star burst (plus), and [D4] recent star burst (three-pointed stars).

The remarkable result is that there is no correlation between the gradients and masses or luminosities in Figure 6. The lack of these relations has already been noticed in the observational data, and the origin of the scatter has been argued (Kobayashi & Arimoto 1999). It seems that more metal-rich simulated ellipticals tend to have steeper gradients, but it is hard to find any relation if simulated dwarfs are included. The origin of scatter is clearly shown with the symbols; the galaxies that form monolithically (filled circles and squares) have steeper gradients, and the galaxies that undergo major mergers (open circles and squares) have shallower gradients. Therefore, we conclude that the metallicity gradients do not depend on the galaxy mass, and the variety of the gradients stems from the difference in the merging history.

The distributions of metallicity gradients for [1] monolithic collapse, [2] assembly, and [3] minor merger are very similar. The minor mergers do not affect so much the metallicity gradients. The distributions for [4] major merger and [5] multiple major mergers are also similar. Then we joint the 5 classes into 2 large classes: [A] non-major merger galaxy including [1]-[3], and [B] major merger galaxy including [4] and [5]. Figure 7 show the histograms of the metallicity gradients for the 2 classes using metallicity Z (top panel), oxygen (middle panel), and iron abundance (bottom panel). The distributions for [A] non-major merger (gray area) and [B] major merger (hatched area) galaxies are different. The typical gradients for non-major merger and major merger galaxies are $\Delta \log Z/\Delta \log r \simeq -0.30$ and -0.22 ,

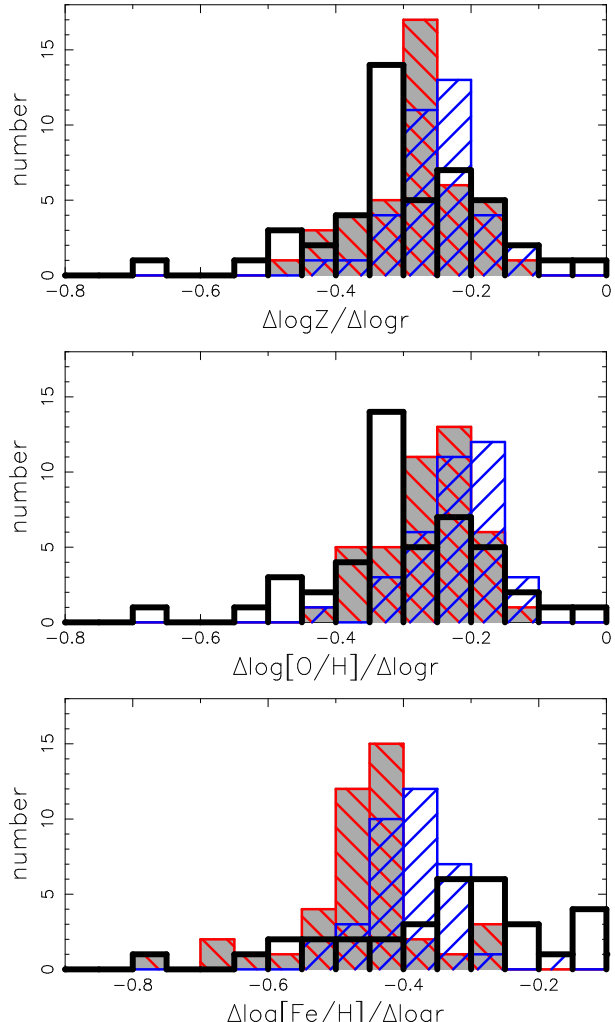


Figure 7. The histograms of the gradients for metallicity Z (upper panel), oxygen (middle panel), and iron abundance (lower panel). The gray and hatched area are for non-major merger (red) and major merger (blue) galaxies, respectively. The thick lines show the observation with Mg_2 (upper and middle panels) or Fe_1 (lower panel) index from Kobayashi & Arimoto (1999).

$\Delta[\text{O}/\text{H}]/\Delta \log r \simeq -0.30$ and -0.18 , and $\Delta[\text{Fe}/\text{H}]/\Delta \log r \simeq -0.45$ and -0.38 , respectively. The galaxies with gradients as steep as $\Delta \log Z/\Delta \log r \leq -0.35$ are all non-major merger galaxies.

The thick lines show the observed metallicity gradient distributions for Mg_2 (top and middle panels) and Fe_1 (bottom panel) using data from Kobayashi & Arimoto (1999). (The reason to compare oxygen gradients with the Mg_2 observation is that the yields relative to solar value are almost the same between O and Mg.) The simulated Z gradients are consistent with the Mg_2 observation both with the mean value of $\Delta \log Z/\Delta \log r \simeq -0.3$ and the dispersion of ± 0.2 . The oxygen gradients are shallower by 0.05 dex than the Mg_2 observation. This is because the Mg_2 index is not a good indicator for magnesium abundance, but rather for metallicity (Tripicco & Bell 1995; Kobayashi & Arimoto 1999). For iron, the simulated Fe gradients are steeper than the observation, even if one takes into account the much larger observational errors of Fe_1 than Mg_2 . This is because in the

simulation the star formation does not terminate completely in the galaxy center (see §4).

From the observed metallicity gradients, we can estimate the fraction non-major merger and major merger galaxies. Using the Mg₂ observation, we derive the numbers of nearby elliptical galaxies with steep gradients of $\Delta \log Z / \Delta \log r \leq -0.3$ and flat gradients of > -0.3 as 25 and 21, respectively. If we take alternative threshold value of $\Delta \log Z / \Delta \log r = -0.25$, the numbers become 30 and 16, respectively. Therefore, the fraction of non-major merger galaxies is half or two third. Even if we take account of some problems involved in our initial condition (see §4 for the detail), there exist non-major merger galaxies and major merger galaxies half and half. The observed variation in the metallicity gradients cannot be explained by either the *monolithic collapse* only or the *major merger* only. It is well reproduced in the present model where both formation processes arise under the CDM scheme.

3.4 EVOLUTION OF GRADIENTS VIA MERGERS

The spatial distribution of metallicity is already shown in the last lines of Figures 2 ([1] the monolithic case) and 3 ([4] the major merger case). The metallicity is enhanced in the high density region, and radial metallicity gradients appear in protogalaxies at $z \sim 5$. After the major merger at $z \simeq 2.0$, many metal-rich stars move to the outer region of the galaxy. In the monolithic case, metal-rich region is concentrated, while metal-rich region extends over ± 10 kpc in the major merger case. The present metallicity gradients are $\Delta \log Z / Z_{\odot} / \Delta \log r = -0.46$ and -0.19 , respectively.

Figures 8 and 9 show the time evolutions of metallicity gradients for [1] the monolithic case and [5] the multiple major merger case, respectively. The thick and thin lines are for the oxygen and iron abundances, respectively. The solid and dotted lines indicate the gradients weighted by V-luminosity and mass, respectively. The gradients are underestimated if the metallicity is weighted by mass.

Figure 8 shows the gradient evolution of ID H3/782389913. This galaxy forms through the assembly of 3 galaxies with the stellar masses of $8 \times 10^9 M_{\odot}$, $4 \times 10^9 M_{\odot}$, and $4 \times 10^9 M_{\odot}$, and thus the initial gradient is not so steep, $\Delta[\text{Fe/H}] / \Delta \log r \simeq -0.9$. This assembly has finished by $z \simeq 3.7$ ($t \simeq 1.2$ Gyr). Then the galaxy evolves quietly, and the metallicity gradient is kept nearly constant. At $z \simeq 0.1$ ($t \simeq 10$ Gyr), a small galaxy with $\sim 10^8 M_{\odot}$ accretes. The small star formation is induced, which changes the gradient by 0.1 dex temporarily.

Figure 9 shows the gradient evolution of ID H3/390367807. This galaxy undergoes the major mergers three times at $z \simeq 1.3, 0.9$, and 0.5 ($t \simeq 3.7, 5.1$, and 6.9 Gyr). The mass ratios are $f = 0.47, 0.16$, and 0.24 , respectively. The initial star burst produces the metallicity gradient of $\Delta[\text{Fe/H}] / \Delta \log r \sim -1.2$. The major merger event is so violent that the gradient decreases by 0.7 dex to be $\Delta[\text{Fe/H}] / \Delta \log r \simeq -0.5$. The second and third merger events are not so active, and the gradient becomes $\Delta[\text{Fe/H}] / \Delta \log r \simeq -0.4$ and -0.3 at the end of the merger event, respectively.

The initial gradient is determined during the initial star burst at $z \gtrsim 3$. The gradient is steeper in the case of quiescent

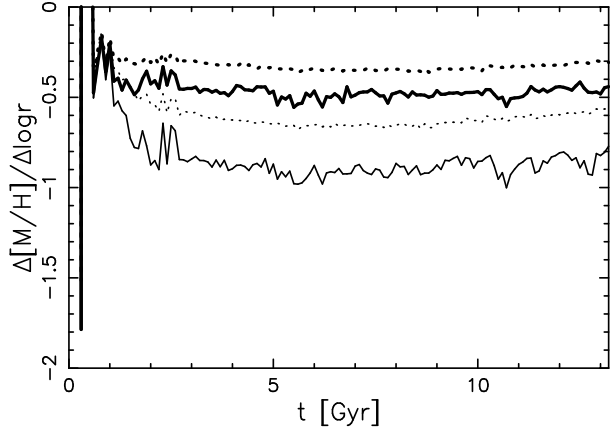


Figure 8. The evolution of metallicity gradients for the monolithic collapse case. The thick and thin lines are for the oxygen and iron abundances, respectively. The solid and dotted lines are the gradients weighted by V-luminosities and masses, respectively.

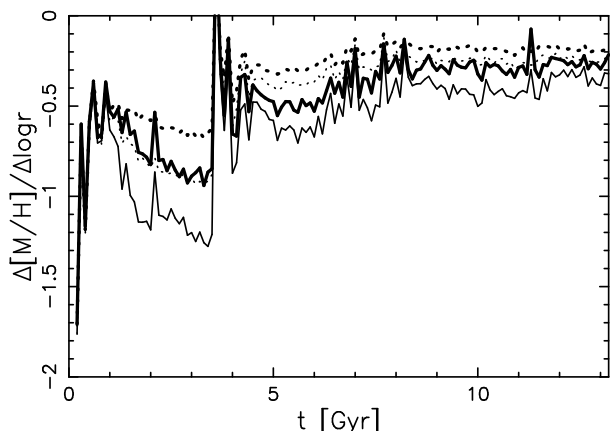


Figure 9. The same as Figure 8, but for the major merger case. Mergers takes place at $t \simeq 3.7, 5.1$, and 6.9 Gyr.

gas accretion, and is shallower in the case of violent assembly of subgalaxies. As a result, the initial gradients span from $\Delta[\text{Fe/H}] / \Delta \log r \simeq -1.5$ to -1.0 . Since the gradients evolve a lot after this time, the initial gradients cannot be inferred from the present gradients.

The metallicity gradients become definitely shallower when galaxies merge. However, the formation and destruction of gradients via mergers are complicated. To find out some rules, we examine the physical conditions at the 151 merging events that occur in our simulations of giant galaxies. Figure 10 shows mass ratios $f \equiv M_2 / M_1$ ($M_1 \geq M_2$) (a), ratios of gas mass $M_{\text{g},2} / M_{\text{g},1}$ (b), gas fractions of primary galaxies $f_{\text{g},1}$ (c), and those of secondary galaxies $f_{\text{g},2}$ (d) against redshifts z . The averages of f and $f_{\text{g},1}$ in each redshift bin decrease toward $z = 0$ because the stellar masses of primary galaxies increase. The average of $M_{\text{g},2} / M_{\text{g},1}$ is larger than that of f , and is constant of ~ 0.5 . $f_{\text{g},2}$ is larger than $f_{\text{g},1}$, and spans from 0 to 1. These are because star formation strongly depends on gas density and takes place slowly in the less-massive secondary galaxies. At $z < 1$, some major mergers ($f \gtrsim 0.2$) have $M_{\text{g},2} / M_{\text{g},1} \gtrsim 0.5$, which means that the secondary galaxies have comparable mass and gas content to the primaries. These induce strong star forma-

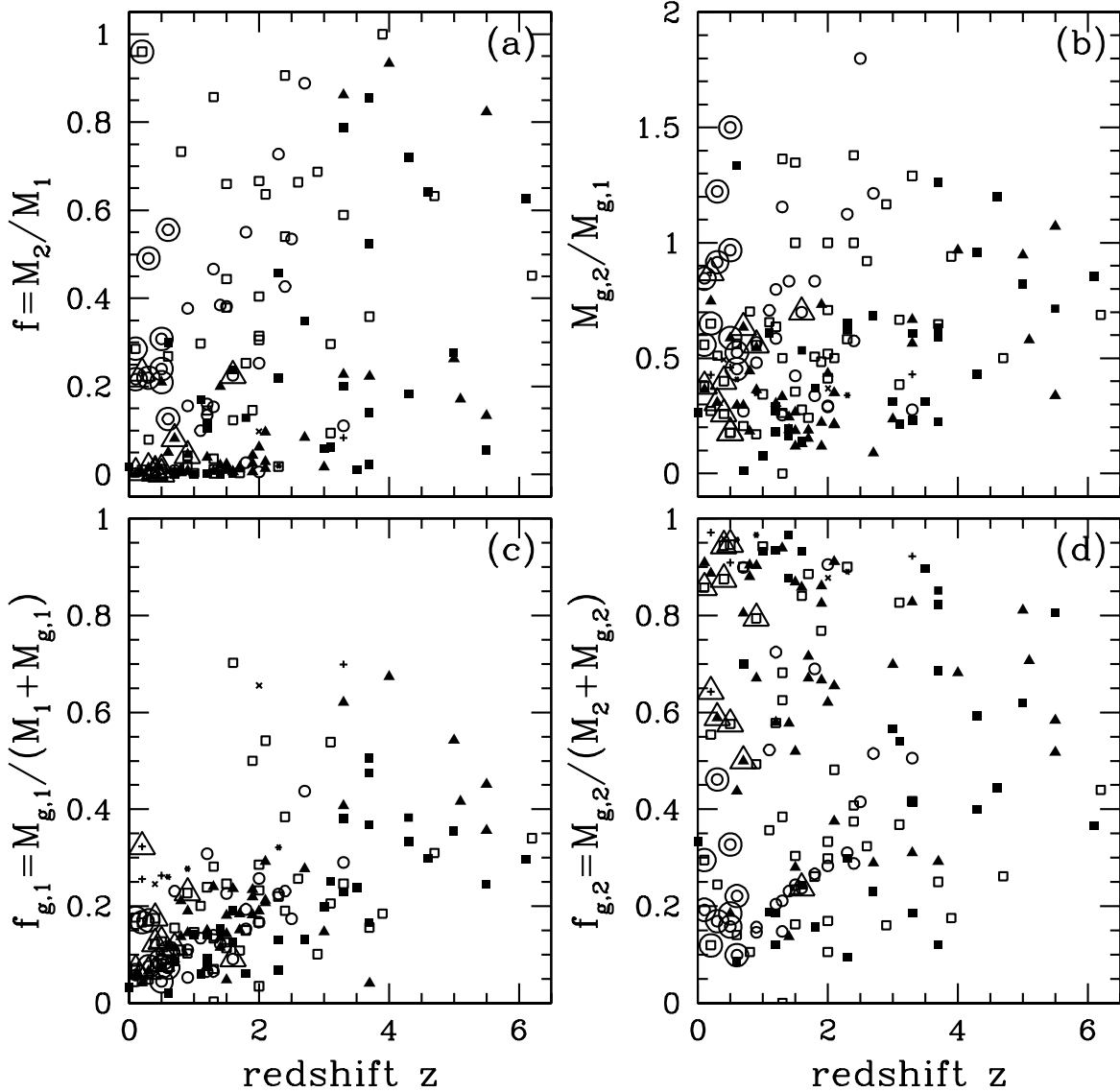


Figure 10. (a) Mass ratios $f \equiv M_2/M_1$ ($M_1 \geq M_2$), (b) ratios of gas mass $M_{g,2}/M_{g,1}$, and (c,d) gas fractions ($f_{g,1}$ and $f_{g,2}$) of the primary and secondary galaxies against redshifts z . For the symbols, see the caption of Figure 6. The points surrounded by large circles/triangles indicate that strong/moderate star formation is induced.

tion (surrounded by circles). Relatively weaker star formation (surrounded by triangles) is induced by mergers with $f_{g,2} \gtrsim 0.5$, which means that the stellar mass of the secondary is small and the secondary galaxy behave like a gas cloud.

Figure 11 shows the change of gradient, $\Delta(\Delta[\text{Fe}/\text{H}]/\Delta \log r)$, caused by a merging event at $z < 3$ against various physical conditions: f (a), $M_{g,2}/M_{g,1}$ (b), $f_{g,1}$ (c), and $f_{g,2}$ (d). The gradient change strongly depends on the mass ratio f . The mergers with $f > 0.2$ decrease the gradients at least by 0.5 dex. This is the reason why we have defined major mergers as those with $f > 0.2$. A major merger changes the orbits of stars. The stars that are in the center and have high metallicities are able to move to the outer region of the galaxy. However, if the secondary

galaxy contains as much gas as the primary galaxy (i.e., $M_{g,2}/M_{g,1} \gtrsim 0.5$) and strong star formation is induced (surrounded by circles), then the gradient change stays smaller than 0.5 dex. This is because such star formation takes place after the gas falls into the center of the primary galaxy and increases the metallicity at the center, resulting in a small gradient change. Sometimes merging of a gas rich galaxy ($f_{g,2} \gtrsim 0.5$) also induces moderate star formation (surrounded by triangles). In this case, star formation takes place in the outer region of the galaxy, and the gradient change can be as large as ~ 0.5 dex, even if $f \sim 0$. In some cases without a merging event, a similar star formation is induced by late gas accretion, and the metallicity gradient gradually becomes shallower.

By showing the similar figure in van Albada (1982), we

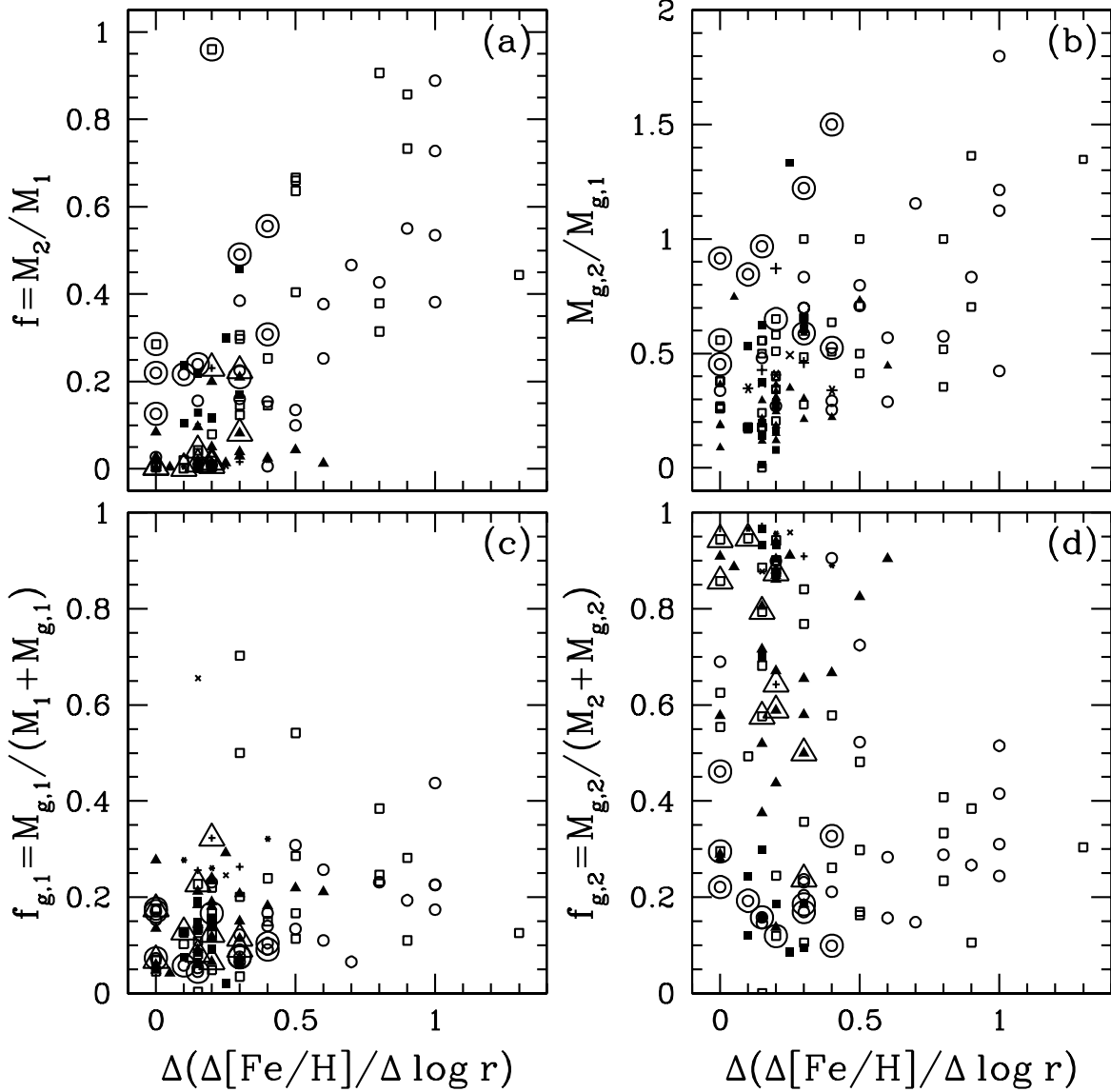


Figure 11. The gradient change $\Delta(\Delta[\text{Fe}/\text{H}]/\Delta \log r)$ before and after the merging event at $z < 3$ against (a) mass ratios f , (b) ratios of gas mass $M_{g,2}/M_{g,1}$, and (c,d) gas fractions ($f_{g,1}$ and $f_{g,2}$). For the symbols, see the caption of Figure 6. The points surrounded by large circles/triangles indicate that strong/moderate star formation is induced.

argue that dynamical information on the orbits of N-body particles is not fully wiped out by a merger, but fairly lost to change the metallicity gradient. Figures 12 and 13 show the energies $E \equiv v^2/2 + \Phi$ of particles before and after a merging event. Large E means that a particle has an extended orbit. Figure 13 shows the energies at 3.5 and 4.9 Gyr for the first major merger at $\simeq 3.7$ Gyr of the galaxy ID H3/390367807 that undergoes a triple major merger (see Figure 9 for the gradient evolution). Figure 12 shows the same but for the non-merger galaxy ID H3/782389913. Clearly, the dispersion for the merger galaxy is much larger than the non-merger galaxy.

In summary, whether the merging event changes the metallicity gradient is mainly influenced by two factors; 1) the mass ratio of the merging galaxies f and 2) the induced

star formation. The evolution of the gradients via merging events is based on the following three processes: i) Destruction by mergers to an extent dependent on f . ii) Regeneration due to the central star formation induced at a rate dependent on $M_{g,2}/M_{g,1}$. iii) Passive evolution as star formation is induced in the outer regions at a rate dependent on $f_{g,2}$. We note that the gradient change is underestimated if the metallicity is weighted not by luminosity as the observation, but by mass as in previous simulations.

4 DISCUSSION

The global properties of elliptical galaxies depend mainly on their masses, while their metallicity gradients are much af-

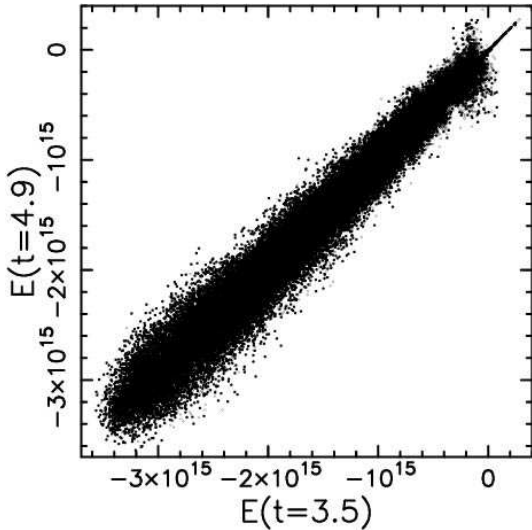


Figure 12. The energies $E \equiv v^2/2 + \Phi$ of particles in the non-merger galaxy.

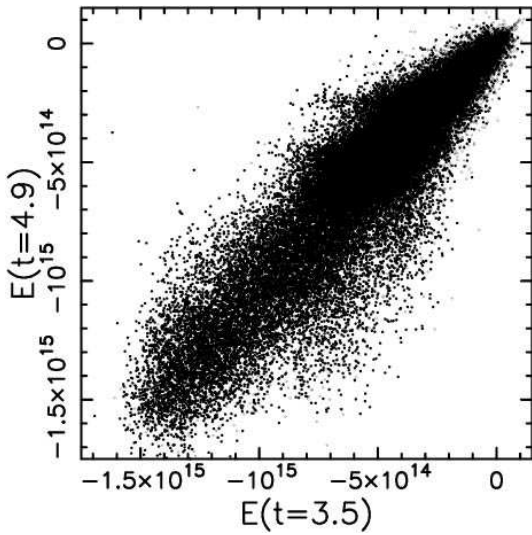


Figure 13. The energies of particles before and after the major merger at ~ 3.7 Gyr.

fected by their merging history. Merging histories can thus, in principle, be inferred from the observed metallicity gradients of present-day galaxies. The dispersion in metallicity gradients for galaxies with similar merging histories is not small (Fig. 7), and so it may be difficult to determine the merging history of an individual galaxy from its metallicity gradient. However, it should be possible to estimate the fractions of non-merger and merger galaxies by using the statistics of metallicity gradients. For example, if the fractions are estimated for field and cluster galaxies, it should provide information about environmental effects on galaxy formation. Even allowing for the uncertainties in available observations of nearby galaxies, our predicted difference between gradients of non-merger and merger galaxies is large enough to be detected.

We should note that there are two problems in the simulated galaxies, which cannot be improved by changing pa-

rameters in the present model. One is that galactic winds do not occur in large galaxies in the simulations, and star formation never terminates completely. The colors of our galaxies thus tend to be bluer than the observation, and the B-V color distribution extends to 0.4 mag bluer. In our galaxy centers, the color gradients tend to have the opposite slope to the metallicity gradients, because the stellar populations there are young. Such late star formation takes place in the central 1 kpc, and this region is carefully excluded when estimating metallicity gradients in this paper. This problem arises from our SPH method and our feedback scheme. If we include the kinetic feedback with $f_{\text{kin}} > 0$, surface brightness decreases at the center, and metal-rich gas blow out. However, these results in too large effective radii and too shallow metallicity gradients to meet the observation. Figure 14 shows the surface brightness profiles and metallicity gradients with (dash-dotted line) and without (solid line) f_{kin} using the same initial condition. With $f_{\text{kin}} = 0.1$, the surface brightness decreases by ~ 2 mag at the center, which results in $r_e = 8.1$ kpc ($r_e = 4.3$ kpc for $f_{\text{kin}} = 0$). The metallicity gradient is almost flat within r_e . To describe galactic winds with the kinetic feedback, star formation scheme should be modified simultaneously.

We note that our predictions for oxygen abundance are not changed so much, whereas the iron abundance should decrease especially at the galaxy center. In Figure 6, there appear to be a relation between the iron abundance and iron gradients. This is because late star formation at the galaxy center increases the iron abundance and steepens iron gradients at the same time. Such a relation can disappear if the galaxy model is improved. In Figure 7, the mean value of simulated iron gradients is steeper than observed. This is also caused by the same reason. If the galaxy model is improved so as to blow a galactic wind, iron gradients for non-merger galaxies will become the similar to their oxygen gradients. However, iron gradients for merger galaxies will be still steeper than oxygen gradients. The difference of iron and oxygen gradients, i.e., $[\text{O}/\text{Fe}]$ gradients, may be the best indicator of the formation history of the galaxy. To discuss $[\text{O}/\text{Fe}]$, observational data of high-enough S/N is required, and the spectral population synthesis models should be prepared for various $[\text{O}/\text{Fe}]$.

The other problem is that simulated galaxies are more extended, and thus there is an offset in the radius-magnitude relation. This problem is not in magnitude, because the Faber-Jackson relation can be reproduced, and the galaxy with given mass has reasonable luminosity. While the stellar mass-to-light ratio is consistent with the observation as $M/L_B \sim 5 - 8$, the total mass-to-light ratio is as large as $(M_{\text{DM}} + M_{\text{baryon}})/L \sim 10 - 100$ (within a sphere of $2r_e$), which may be too large. The baryon fraction increases to ~ 0.5 at the center ($r < 1$ kpc) because of the stellar concentration, but is as small as ~ 0.2 in $r < 2r_e$. Baryon does not fully dominate even at the galaxy center in our simulated galaxies, and the stellar concentration seems to be not enough compared with the dark matter concentration. These might be due to cosmological parameters, dynamical friction, star formation parameter, and the limited field size of initial condition. As well known with the zero-point offset in the Tully-Fisher relation (Navarro & Steinmetz 2000), such high dark matter concentration should arise from the standard CDM cosmology that is adopted in this paper, and

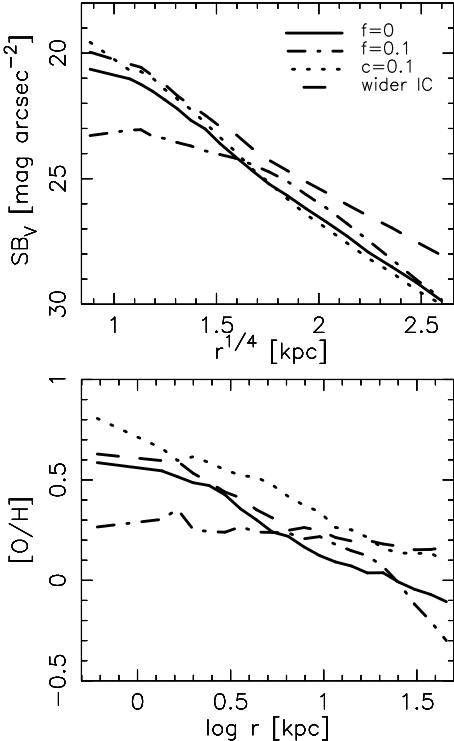


Figure 14. Surface brightness profiles (upper panel) and metallicity gradients (lower panel) with kinetic feedback (dash-dotted line, $f_{\text{kin}} = 0.1$), with longer timescale of the star formation (dotted line, $c = 0.1$), and wider region of initial condition (2.5 Mpc).

should decrease to some extent with the λ -CDM cosmology. However, Navarro & Steinmetz (2000) argued that the zero-point offset remains even with the λ -CDM cosmology, which requires substantial revision to the CDM scenario such as σ_8 , a tilt in the primordial power spectrum, or hot dark matter. The dynamical friction may be effective because the mass of a dark matter particle is ten times larger than the gas and stellar particles (but see Steinmetz & White 1997). Too large effective radius suggests that the star formation takes place too early before the gas accretes towards the center. This can be solved by changing the star formation timescale, i.e., reducing the star formation parameter c , although colors become bluer. As shown in Figure 14, with $c = 0.1$ (dotted line), the surface brightness increase by 1 mag at the center, which results in smaller effective radius as $r_e = 3.2$ kpc. The metallicity increases because of longer timescale of star formation, but the gradient does not change so much. As mentioned in §3.2, the surface brightness profiles of our simulated galaxies well follow the de-Vaucouleurs law, but is smeared out at the center, and the central surface brightness ($r < 1$ kpc) is slightly smaller than the de-Vaucouleurs fit (see Fig.14). Although the resolution is not enough to discuss, this central stellar concentration may be smaller than other simulations (e.g., Springel & Hernquist 2003), can be as large with $c = 0.1$, and should be affected by the difference in the star formation and feedback schemes.

The initial condition is most important. The edge of the simulated fields actually falls into a galaxy at $z \sim 2 - 4$ depending on the position of the galaxy in the field. The galaxy mass M_{200} (the mass with higher density than $200\rho_{\text{crit}}$) stops

increasing at $z \sim 1.5 - 3$. This means that there is an artificial cutoff of mass accretion around this redshift, which results in the cutoff of star formation rate in Figure 4. In a wider simulation with a radius of ~ 2.5 Mpc (dashed-line in Fig.14) instead of ~ 1.5 Mpc in the series of our simulation, the star formation continues longer, and thus colors tend to be too blue. The total luminosity becomes ~ 2 times larger, but still ~ 3 times smaller than the observation. With much wider simulation, the luminosity difference could be improved, but the color inconsistency becomes much larger, and such galaxy is no more elliptical. The star formation and feedback schemes need to be modified accordingly, such as some recent works have tried (e.g., Springel & Hernquist 2003). In this paper, the mass accretion and star formation are truncated artificially by the initial condition. However, in observed ellipticals, star formation should be truncated at $z \sim 2$ by some process; tidal stripping, effects of active galactic nuclei, and so on. This epoch may correspond to the epoch when the galaxy falls into a cluster, because the galaxy moves too fast to arise mass accretion.

If we include the contribution of the outside of the simulated field, late accretion and late merging events should increase. Both make the metallicity gradient shallow. As noted in §2.3, fields with larger spin parameter λ are not included in our simulation, and an elliptical can form through major mergers of disk galaxies in some of such fields. However, as shown in Figure 7, the predicted metallicity gradients are already in good agreement with the observation, and the increase of merger galaxies conflicts with the observation. If star formation and feedback schemes improved, evolution of metallicity gradients may also be affected at some extent. We should note, however, that the following conclusions will not change; major merger make the metallicity gradients shallow, and there should be non-merger ellipticals to explain the observed steep gradients.

5 CONCLUSIONS

We study the formation and chemodynamical evolution of galaxies with our GRAPE-SPH chemodynamical model that includes various physical processes associated with the formation of stellar systems; radiative cooling, star formation, feedback from SNe II, SNe Ia, and SWs, and chemical enrichment. We simulate 72 slowly-rotating spherical fields (spin parameter $\lambda \sim 0.02$), and obtain 124 galaxies (78 ellipticals and 46 dwarfs) from the CDM initial fluctuation. All simulated galaxies have the de Vaucouleurs' surface brightness profiles, and are therefore elliptical galaxies. Most stars in ellipticals form during the initial star burst at $z \gtrsim 2$, while dwarfs undergo relatively continuous star formation. In our scenario, galaxies form through the successive merging of sub-galaxies. The merging history is various and the difference is seeded in the initial conditions. In some cases, galaxies form through the assembly of gas rich small galaxies, and the process looks like a *monolithic collapse*. In other cases, the evolved galaxies undergo *major merger* of galaxies. Major mergers are defined as those with the mass ratios of the primary and secondary galaxies being $f \gtrsim 0.2$.

We examine the physical conditions during 151 merging events that occur in our simulation. Whether the merging event changes the metallicity gradient is mainly influenced

by two factors; the mass ratio of the merging galaxies f and the induced star formation. The basic processes of the formation and evolution of the gradients are summarized below:

- Formation of initial gradients — The initial gradient is determined from the initial star burst at $z \gtrsim 3$. The gradient is steeper in the case of quiescent gas accretion, and is shallower in the case of violent assembly of subgalaxies. As a result, the initial gradients span from $\Delta[\text{Fe}/\text{H}]/\Delta \log r = -1.5$ to -1.0 .
- Destruction by mergers — The major merger changes the orbits of stars. The metal-rich stars at the center are able to move to the outer region of the galaxy. The gradient change is determined mainly from the mass ratio of merging galaxies f . With larger f , the gradients become shallower. If the mass ratio of merging galaxies is larger than $f \sim 0.2$, the gradient change is larger than ~ 0.5 dex.
- Regeneration due to the induced star formation — If the ratio of gas mass is as large as $M_{\text{g},2}/M_{\text{g},1} \gtrsim 0.5$, strong star formation is induced at the center of the primary galaxy, and the gradient change is smaller than ~ 0.5 dex.
- Passive evolution — If the gas fraction of the secondary galaxy is larger than $f_{\text{g},2} \sim 0.5$, moderate star formation is induced in the outer region of the primary galaxy, and the gradient change becomes as large as ~ 0.5 dex, even if $f \sim 0$. In some case without merging event, if the similar star formation is induced by the late gas accretion, the metallicity gradient gradually becomes shallower.

We succeed in reproducing the observations of metallicity gradients and finding the origin of the variety of internal structures. From the distribution functions of the gradients for different merging histories, we discuss the origin of elliptical galaxies.

- The average metallicity gradient is $\Delta \log Z/\log r \simeq -0.3$ and the dispersion is ± 0.2 , which are both consistent with observations of Mg₂ gradients.
- No correlation is produced between gradients and masses. The metallicity gradients do not depend on the galaxy mass, and the variety of the gradients stems from the difference in the merging histories; galaxies that form monolithically have steeper gradients, while galaxies that undergo major mergers have shallower gradients.
- The metallicity gradient distributions for [A] non-major merger ([1]-[3]) and [B] major merger galaxies ([4] and [5]) are quite different. The typical gradients for non-major merger and major merger galaxies are $\Delta \log Z/\Delta \log r \sim -0.3$ and -0.2 , respectively. Simulated galaxies with the gradients steeper than -0.35 are all non-major merger galaxies.

The global properties of elliptical galaxies depend mainly on their masses, while their metallicity gradients are much affected by their merging history. A major merger makes the gradient shallower. Therefore, merging histories can be inferred from the observed metallicity gradients of present-day galaxies. Available observations for nearby galaxies suggest that there exist non-major merger galaxies and major merger galaxies half and half. The observed variation in the metallicity gradients cannot be explained by either *monolithic collapse* or by *major merger* alone. Instead, it is well reproduced in the present model in which both formation processes arise under the CDM scheme.

ACKNOWLEDGMENTS

This paper is a part of the Ph.D. thesis of C. Kobayashi in the Astronomy Department of the University of Tokyo. I would like to thank the supervisor, K. Nomoto and the advisor, N. Arimoto. I am grateful to N. Nakasato, J. Makino, M. Mori, T. Kodama, N. Tamura, K. Ohta, V. Springel, F. van den Bosch, and A. Renzini for fruitful discussion, and S.D.M. White for detailed suggestion. I also thank to the Japan Society for Promotion of Science for a financial support, and to National Observatory of Japan for the GRAPE-5 MUV system.

REFERENCES

Abbott, D. C. 1982, ApJ, 263, 723
 Arimoto, N., & Yoshii, Y. 1987, A&A, 173, 23
 Bacon, R., et al. 2001, MNRAS, 326, 23
 Balsara, D. S. 1995, J. Chem. Phys., 121, 357
 Bargar, A. J., Cowie, L. L., Trentham, N., Fulton, E., Hu, E. M., Songaila, A., & Hall, D. 1999, AJ, 117, 102
 Barnes, J. E. 1988, ApJ, 331, 699
 Barnes, J. E. 1996, in IAU Symp. 171, New Light on Galaxy Evolution, p.191
 Baugh, C. M., Cole, S., & Frenk, C. S. 1996, MNRAS, 283, 1361
 Bender, R., & Surma, P. 1992, A&A, 258, 250
 Benson, A. J., Ellis, R. S., & Menanteau, F. 2002, MNRAS, 336, 564
 Benz, W., Bowers, R., Cameron, A., Press, W. 1990, ApJ, 348, 647
 Bertschinger, E. 1987, ApJ, 323, L103
 Bertschinger, E. 1995, <http://arcturus.mit.edu/cosmics/>
 Bower, R. G., Lucey, J. R., & Ellis, R. S. 1992, MNRAS, 254, 601
 Blinnikov, S., Lundqvist, P., Bartunov, O., Nomoto, K., & Iwamoto, K. 2000, ApJ, 532, 1132
 Brinchmann, J., & Ellis, R. S. 2000, ApJ, 536, L77
 Carlberg, R. G. 1984, ApJ, 286, 403
 Carollo, C. M., Danziger, I. J., & Buson, L. 1993, MNRAS, 265, 553
 Carraro, G., Lia, C., & Chiosi, C. 1998, MNRAS, 297, 1021
 Cimatti, A. et al. 2002, A&A, 391, L1
 Ciotti, L., D'Ecole, A., Pellegrini, S., & Renzini, A. 1991, ApJ, 376, 380
 Cole, S., Aragón-Salamanca, A., Frenk, C. S., Navarro, J. F., & Zepf, S. E. 1994, MNRAS, 271, 781
 Cole, S., Lacey, C. G., Baugh, C. M., & Frenk, C. S. 2000, MNRAS, 319, 168
 Daddi, E., Cimatti, A., & Renzini, A. 2000, A&A, 362, L45
 David, L. P., Forman, W., & Jones, C. 1990, ApJ, 459, 29
 Davies, R. L., Burstein, D., Dressler, A., Faber, S. M., Lynden-Bell, D., Terlevich, R. J., & Wegner, G. 1987, ApJS, 64, 581
 Davies, R. L., Sadler, E. M., & Peletier, R. F. 1993, MNRAS, 262, 650
 de Vaucouleurs, G. 1961, ApJS, 5, 233
 Dickinson, M. 1996, in ASP Conference Series, 86, Fresh Views of Elliptical Galaxies, eds., A.Buzzoni, A.Renzini, & A.Serrano, p.283
 Dickinson, M., Papovich, C., Ferguson, H. C., & Budavári, T. 2003. astro-ph/0212242

Djorgovski, S., & Davis, M. 1987, *ApJ*, 313, 59

Dressler, A. 1980, *ApJ*, 236, 351

Dressler, A., Lynden-Bell, D., Burstein, D., Davies, R. L., Faber, S. M., Terlevich, R. J., & Wegner, G. 1987, *ApJ*, 313, 42

Dressler, A., Oemler, A., Couch, W. J., Smail, I., Ellis, R. S., Barger, A., Butcher, H., Poggianti, B. M., & Sharples, R. M. 1997, *ApJ*, 490, 577

Drory, N., Bender, R., Snigula, J., Feulner, G., Hopp, U., maraston, C., Hill, G. J., & Menndes de Oliveira, C. 2001, *ApJ*, 562, L111

Efstathiou, G., Davis, M., Frenk, C. S., & White, S. D. M. 1985, *ApJS*, 57, 241

Evrard, A. E. 1988, *MNRAS*, 235, 911

Faber, S. M. 1973, *ApJ*, 179, 731

Faber, S. M. 1977, in *The Evolution of Galaxies and Stellar Populations*, ed. B.T. Tinsley, & R. B. Larson (New Heaven:Yale Univ. Press), p.157

Fontana, A., Menci, N., D'Odorico, S., Giallongo, E., Poli, F., Cristiani, S., Moorwood, A., & Saracco, P. 1999, *MNRAS*, 310, L27

Franceschini, A., Silva, L., Fasano, G., Granato, G. L., Bressan, A., Arnouts, S., & Danese, L. 1998, *ApJ*, 506, 600

Gingold, R. A., & Monaghan, J. J. 1977, *MNRAS*, 181, 375

Greggio, L., & Renzini, A. 1983, *A&A*, 118, 217

González, J. J., & Gorgas, J. 1996, in *ASP Conference Series*, 86, *Fresh Views of Elliptical Galaxies*, eds., A.Buzzoni, A.Renzini, & A.Serrano, p.225

Gorgas, J., Efstathiou, G., & Aragón-Salamanca, A. 1990, *MNRAS*, 245, 217

Gott, J. R. 1973, *ApJ*, 186, 481

Gott, J. R. 1975, *ApJ*, 201, 296

Habe, A., & Ohta, K. 1992, *PASJ*, 44, 203

Hernquist, L., & Katz, N. 1989, *ApJS*, 70, 419

Im, M. et al. 2002, *ApJ*, 571, 136

Katz, N. 1992, *ApJ*, 391, 502

Katz, N., Weinberg, D. H., & Hernquist, L. 1996, *ApJS*, 105, 19

Kauffmann, G. 1996, *MNRAS*, 281, 487

Kauffmann, G., & Charlot, S. 1998, *MNRAS*, 294, 705

Kauffmann, G., White, S. D. M., & Guiderdoni, B. 1993, *MNRAS*, 264, 201

Kawata, D., & Gibson, B. K. 2003, *astro-ph/0212401*

Kelson, D. D., van Dokkum, P. G., Franx, M., Illingworth, G. D., & Fabricant, D. 1997, *ApJ*, 478, L13

Kennicutt, Jr. R. C. 1983, *ApJ*, 272, 54

Kennicutt, Jr. R. C. 1989, *ApJ*, 344, 685

Kobayashi, C., 2002, *PhD thesis*, Univ. of Tokyo

Kobayashi, C., & Arimoto, N. 1999, *ApJ*, 527, 573

Kobayashi, C., Tsujimoto, T., Nomoto, K., Hachisu, I., & Kato, M. 1998, *ApJ*, 503, L155

Kobayashi, C., Tsujimoto, T., & Nomoto, K. 2000, *ApJ*, 539, 26

Kodama, T. 1997, Ph.D. Thesis. University of Tokyo

Kodama, T., & Arimoto, N. 1997, *A&A*, 320, 41

Kodama, T., Arimoto, N., Barger, A.J., & Aragón-Salamanca, A. 1998a, *A&A*, 334, 99

Larson, R. B. 1974a, *MNRAS*, 166, 585

Larson, R. B. 1974b, *MNRAS*, 169, 229

Larson, R. B. 1975, *MNRAS*, 173, 671

Lattanzio, C., Monaghan, J., Pongracic, H., & Schwarz, P. 1985, *MNRAS*, 215, 125

Leitherer, C., Robert, C., & Drissen, L. 1992, *ApJ*, 401, 596

Low, C., & Lynden-Bell, D. 1976, *MNRAS*, 176, 367

Lucy, L. 1977, *AJ*, 82, 1013

Lynden-Bell, D. 1967, *MNRAS*, 136, 101

Marchant, A. B., & Shapiro, S. L. 1977, *ApJ*, 215, 1

Matteucci, F. 1996, *Fundamentals of Cosmic Phisics* Vol.17, p.283

Menanteau, F., Ellis, R. S., Abraham, R. G., Barger, A. J., & Cowie, L. L. 1999, *MNRAS*, 309, 208

Mosconi, M. B., Tissera, P. B., Lambas, D. G., & Cora, S. A., 2001, *MNRAS*, 325, 34

Monaghan, J. J. 1992, *ARA&A*, 30, 534

Monaghan, J. J., & Gingold, R. A. 1983, *J. Comput. Phys.*, 52, 374

Monaghan, J. J., & Lattanzio, C. 1985, *A&A*, 149, 135

Nakasato, N. 2000, *PhD thesis*, Univ. of Tokyo

Nakasato, N., & Nomoto, K. 2003, *ApJ*, in press (*astro-ph/0301404*)

Navarro, J. F., & Steinmetz, M. 1997, *ApJ*, 478, 13

Navarro, J. F., & Steinmetz, M. 2000, *ApJ*, 538, 477

Navarro, J. F., & White, S. D. M. 1993, *MNRAS*, 265, 271

Navarro, J. F., & White, S. D. M. 1994, *MNRAS*, 267, 401

Nomoto, K., Hashimoto, M., Tsujimoto, T., Thielemann, F. -K, Kishimoto, N., Kubo, Y., & Nakasato, N. 1997a, *Nuclear Physics*, A616, 79c

Nomoto, K., Iwamoto, K., Nakasato, N., Thielemann, F. -K, Brachwitz, F., Tsujimoto, T., Kubo, Y., & Kishimoto, N. 1997b, *Nuclear Physics*, A621, 467c

Nomoto, K., Thielemann, F. -K, & Yokoi, K. 1984, *ApJ*, 286, 644

Raiteri, C. M., Villata, M., & Navarro, J. F., *A&A*, 315, 105

Renzini, A. 2002, in *ASP Conference Series*, 253, *Chemical Enrichment of Intracluster and Intergalactic Medium*, eds., R. Fusco-Femiano & F. Matteucci, p.331

Salpeter, E. E. 1955, *ApJ*, 121, 161

Schade, D., Barrientos, L. F., & Lopez-Cruz, O. 1997, *ApJ*, 477, L17

Schade, D., et al. 1999, *ApJ*, 525, 31

Schmidt, M. 1959, *ApJ*, 129, 243

Schweizer, F., & Seitzer, P. 1992, *AJ*, 104, 1039

Schweizer, F., Seitzer, P., Faber, S. M., Burstein, D., Ore, C. M. D., & Gonzalez, J. J. 1990, *ApJ*, 364, L33

Silk, J. 1977, *ApJ*, 214, 718

Silva, D. R., & Bothun, G. D. 1998, *AJ*, 116, 85

Springel, V. & Hernquist, L. 2003, *MNRAS*, 339, 289

Stanford, S. A., Eisenhardt, P. R. M., & Dickinson, M. 1998, *ApJ*, 492, 461

Steinmetz, M. 1996, *MNRAS*, 278, 1005

Steinmetz, M., & Müller, E. 1994, *A&A*, 281, L97

Steinmetz, M., & Navarro, J. F. 2002, *New Astronomy*, 7, 155

Steinmetz, M., & White, S. D. M. 1997, *MNRAS*, 288, 545

Sugimoto, D., Chikada, Y., Makino, J., Ito, T., Ebisuzaki, T., & Umemura, M. 1990, *Nature*, 345, 33

Sutherland, R. S., & Dopita, M. A. 1993, *ApJS*, 88, 235

Thomas, P. A., & Couchman, H. M. P. 1992, *MNRAS*, 257, 11

Tinsley, B. M. 1980, Fundamentals of Cosmic Phisics Vol.5, p.287

Toomre, A., & Tommre, J. 1972, ApJ, 178, 623

Toomre, A. 1977, in The Evolution of Galaxies and Stellar Populations, ed. B. M. Tinsley and R. B. Larson (New Haven: Yale University Observatory), p.401

Tripicco, M. J., & Bell, R. A. 1995, AJ, 110, 3035

van Dokkum, P. G., & Franx, M. 1996, MNRAS, 281, 985

van Dokkum, P. G., & Franx, M. 2001, ApJ, 553, 90

Umemura, M., Fukushige, T., Makino, J., Ebisuzaki, T., Sugimoto, D., Turner, E., & Loeb, A. 1993, PASJ, 45, 311

van Albada, T. S., 1982, MNRAS, 201, 939

Warren, M. S., Quinn, P. J., Salmon, J. K., & Zurek, W. H. 1992, ApJ, 399, 405

White, S. D. M. 1980, MNRAS, 191, 1p

White, S. D. M. 1978, MNRAS, 184, 185

Woosley, S. E., & Weaver, T. A. 1995, ApJS, 101, 181

Zel'dovich, Ya. B. 1970, A&A, 5, 84

Zepf, S. E. 1997, Nature, 390, 377

This paper has been typeset from a \TeX / \LaTeX file prepared by the author.